



# City Research Online

## City St George's, University of London

**Citation:** Khan, K., Chen, Z., Liu, J., Tsavdaridis, K. D. & Poologanathan, K. (2023). Axial compression behaviors of steel shear-keyed tubular columns: Numerical and analytical studies. *Journal of Constructional Steel Research*, 205, 107894. doi: 10.1016/j.jcsr.2023.107894

This is the accepted version of the paper.

This version of the publication may differ from the final published version. To cite this item please consult the publisher's version.

**Permanent repository link:** <https://openaccess.city.ac.uk/id/eprint/30434/>

**Link to published version:** <https://doi.org/10.1016/j.jcsr.2023.107894>

**Copyright and Reuse:** Copyright and Moral Rights remain with the author(s) and/or copyright holders. Copies of full items can be used for personal research or study, educational, or not-for-profit purposes without prior permission or charge, unless otherwise indicated, provided that the authors, title and full bibliographic details are credited, a hyperlink and/or URL is given for the original metadata page and the content is not changed in any way. For full details of reuse please refer to [City Research Online policy](#).

# Axial compression behaviors of steel shear-keyed tubular columns: Numerical and analytical studies

Kashan Khan<sup>a</sup>, Zhihua Chen<sup>a,b,c</sup>, Jiadi Liu<sup>a</sup>, Konstantinos Daniel Tsavdaridis<sup>d</sup>,  
Keerthan Poologanathan<sup>e</sup>

<sup>a</sup>Department of Civil Engineering, Tianjin University, Tianjin, China

<sup>b</sup>State Key Laboratory of Hydraulic Engineering Simulation and Safety, Tianjin, China

<sup>c</sup>Key Laboratory of Coast Civil Structure and Safety, Tianjin University, Tianjin, China

<sup>d</sup>School of Science & Technology, Department of Engineering, City, University of London (UK)

<sup>e</sup>Department of Mechanical and Construction Engineering, Northumbria University (UK)

**Abstract:** This study developed a finite element model (FEM) and reported parametric and analytical studies on the axial compression behaviors of shear-keyed tubular columns in modular steel structures (MSS). The accuracy of the developed FEM was validated using 36 tests in references. The parametric study designed 108 FEMs to investigate initial imperfection, shear-key height ( $L_t$ ), thickness ( $t_t$ ), steel tube length ( $D$ ), width ( $B$ ), thickness ( $t_c$ ), and height ( $L_c$ ) influence. The typical load-shortening response showed elastic, inelastic, and recession stages, with failure modes of inward and outward sinusoidal pairs of local buckling. Increasing  $t_t$ ,  $L_t$ ,  $t_c$ ,  $D$ , or  $B$  improved strength and stiffness, while  $L_c$  or slenderness ( $L_c/r$ ) adversely affected the stiffness and ductility linearly. Besides, it ensured by validations that prediction equations in conventional design standards overestimated the compressive resistance, requiring modifications.

**Keywords:** Axial compression behaviors; Steel shear-keyed tubes; Finite element modeling; Experimental validations; Prediction equations

## 28 **1 Introduction**

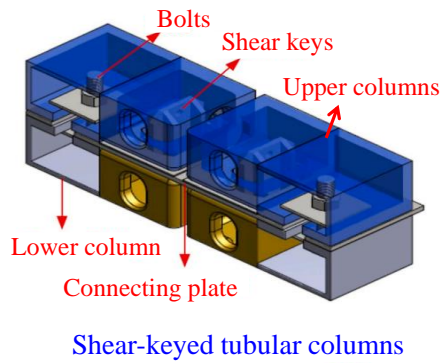
29 Modular steel structure (MSS) comprises an onsite assembly of ready-made room-sized  
30 volumetric modules [1]. It has shown time efficiency [2], cost-effectiveness [3], high  
31 quality [4], improved safety [5], and reduced environmental impacts [6]. Column  
32 discontinuity distinguishes it from traditional steel structures (TSS) [7]. Corner-  
33 supported load-bearing steel modules resist loads via corner columns, providing space  
34 flexibility and a clear load transfer path [8–10]. Thus, they can extend to multi-story  
35 structures, as depicted in **Fig. 1(a)** [3,11]. They achieve outstanding strength, ductility,  
36 robustness, rigidity, durability, and lightness via steel-hollow section (SHS) columns to  
37 withstand loads [12–14]. The structural behavior and integrity of MSS mainly rely on  
38 the modules and their deformation coordination [15], ensured by a reliable inter-  
39 modular connection (IMC) [16]. Hence, welded [17], bolted [16], and pre-stressed  
40 [18,19] IMC are used at modules' corners to achieve structural integrity. However,  
41 technical difficulties, such as the robustness, instability, and complexity of interior  
42 connection tying, require effective measures because weak IMCs can affect the MSS's  
43 safety [20,21]. Thus, numerous joints between SHS columns have been proposed to  
44 address these concerns. Studies have been summarized in recently published review  
45 articles on IMC [1,16,22–27].

46 The shear-keyed IMC provides robust and efficient module connectivity at corners.  
47 Chen et al. [28,29], Khan et al. [30–32], and Peng et al. [33–36] applied non-welded  
48 hollow-shaped shear-keyed IMC in multi-story corner-supported MSS, demonstrating  
49 its applicability in real projects, as shown in **Fig. 1(a,b)**. Several welded, non-welded,  
50 or bolted shear-keyed IMC, including the solid or hollow box, threaded, cruciform, or  
51 socket-shaped join columns to ensure appropriate module connectivity and eliminate  
52 discreteness, are listed in Ref. [26]. Besides, different shear-keyed tubes and IMC have

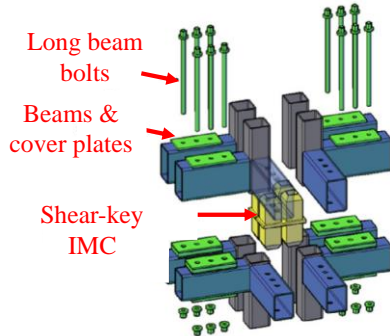
53 been studied, including experimental research by Hajimohammadi et al. [37]. They  
54 observed that raising the loading angle from  $0^0$  to  $45^0$  reduces shear keys' ultimate  
55 resistance, turning ASME-B1.1, BS-3580, and ISO/TR-16224 unsuitable. Chen et al.  
56 [28,29] discovered that shear-keyed IMC causes column tearing due to the shear and  
57 bending stresses. Bowron [38], Khan et al. [30–32], and Pang et al. [39] found non-  
58 welded and fully-bolted shear keys as semi-rigid while offering horizontal connectivity  
59 to columns. However, columns at shear-key zones generated significant stresses. The  
60 grouted shear-keyed tube was discovered by Dai et al. [40,41] to resist a load rigidly.  
61 Ma et al. [42], Deng et al. [43], and Zhang et al. [44] observed that shear resistance was  
62 offered by welded and bolted shear keys, but the absence of interior module fixity  
63 resulted in their rotations around columns. Nadeem et al. [45] presented an IMC with a  
64 self-locking shear key. They witnessed good resistance to slip and lateral forces [37].  
65 However, geometrical imperfections causing installation issues were disregarded,  
66 impacting tube buckling behavior [9]. Welded [46] or bolted [47] shear-keyed tubes'  
67 lateral performance revealed adequate uplift resistance, ductility, and continuity to  
68 columns. Still, column tearing and beam-column connection failure was noticeable.  
69 Recently, research focused on post- and pre-stressed shear-keyed IMC. For instance,  
70 Liew et al. [48,49] and Chen et al. [18] noted that shear-keyed IMC effectively provides  
71 lateral load resistance. Sanches et al. [50,51] determined that shear-key thickness  
72 governs the shear-keyed tube lateral force resistance through friction. Sandblasting or  
73 expanding the contact area increases the shear-slip resistance of shear-keyed tubes, as  
74 per Lacey et al. [52,53]. Although investigations mainly focused on lateral behavior, it  
75 can be seen that most shear-keyed IMC used shear keys inside tubes without welding  
76 or bolting. They observed that lateral and shear resistance was affected by the shear-  
77 key thickness and cross-section; however, shear-keyed tube axial compression behavior

78 is unclear. Typically, buckling resistances and joint rotation are ignored, assuming  
79 shear keys and columns are tightly welded, leading to a conservative design. Because  
80 they have been studied and used in MSS projects, compression investigations on non-  
81 welded shear-keyed tubes are necessary.

82 Modules integrated with SHS using shear keys exhibit superior structural performance  
83 compared to cold-formed C-sections [1,2]. Traditional standards yielded conservative  
84 outcomes on the compression behavior of cold-formed columns [54]; however, Khan  
85 et al. [12–14] verified non-conservative findings for hot-rolled MSS tubular walls.  
86 Significant research has been performed on the tubes' compressive behavior. Still, their  
87 assumptions and conclusions were exclusive to TSS standard tubes with continuity at  
88 both or one end. Conversely, MSS's integrated modules cause tube discontinuities.  
89 Moreover, the studies above provide little information on shear-keyed tubes, which  
90 results in different boundary conditions, effective lengths, critical load, and ultimate  
91 resistance [55]. Unless unique details are not accounted for, conventional standards  
92 compatibility for shear-keyed columns becomes questionable. Additionally, tube  
93 designs disregarding shear-keyed IMC are unsuitable because they do not account for  
94 varying flexural rigidities of tubes at the mid-height and ends. Hence, this study  
95 investigated the shear-keyed columns' axial compression behaviors by developing a  
96 finite element model (FEM) and validating its accuracy with the 36 tests on standard  
97 and shear-keyed tubes. The influence of initial imperfection, shear-key height and  
98 thickness, and steel tube length, width, thickness, and height was investigated. Finally,  
99 traditional design standards' predictions applicability was examined to evaluate the  
100 ultimate resistances of shear-keyed tubes.

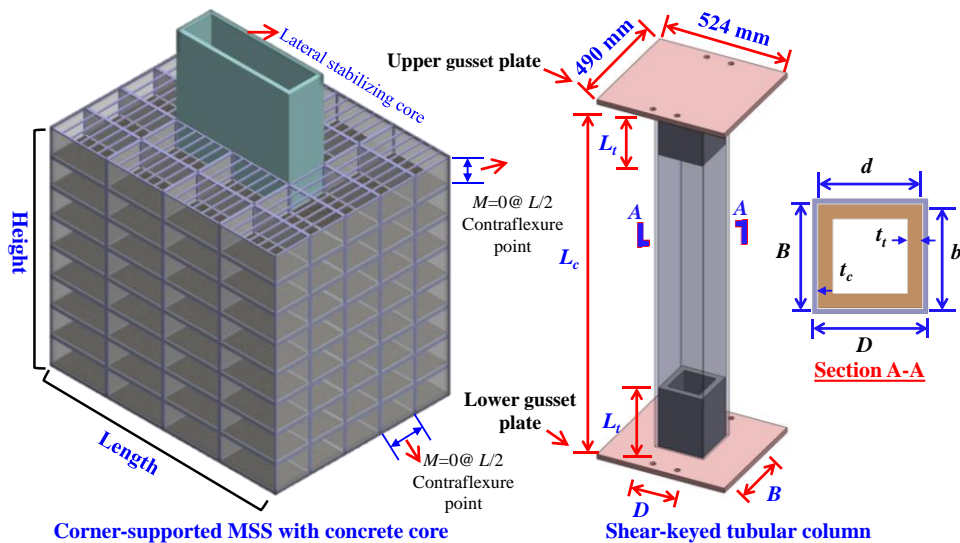


Haoshi office building, Tangshan, China



Tianjin Ziya office building, Tianjin, China

(a) Corner-supported modules with shear-keyed IMC (Designed by the research team) [28,29]



Corner-supported MSS with concrete core

Shear-keyed tubular column

(b) Typical MSS with shear-keyed tubular columns details under consideration

**Fig. 1** Applications of corner-supported MSS with shear-keyed tubes

## 2 Literature on experimental studies on SHS tubes

### 2.1 Combined axial and lateral loading

Chen et al. [28,29] evaluated shear-keyed IMC structural behavior with axial and lateral loadings on 12 shear-keyed frames. The axial and lateral loads were applied to the top free column via the column loading technique, with the lower column, ceiling, and floor beams functioning as rotational hinges. **Table 1** shows specimen details.

113 **2.2 Axial compression loading**

114 Theofanous and Gardner [56,57] conducted compression tests on stubs and flexural  
 115 tests on long tubes. Stubs were fixed, while long tubes were pin-ended. Hou et al. [58]  
 116 and Khan et al. [12,13] compressed planar and C-shaped walls having five tubes in  
 117 planar, whereas additional three tubes in the C-shaped sidewalls. A ceiling beam, angle  
 118 support, and a floor beam were welded to tubes. Welded blocks were installed on the  
 119 bolted ceiling and the floor beam to create pin-ended boundaries. All specimen details  
 120 are depicted in **Table 2**.

**Table 1** Specifications and results of combined axial and lateral loading on tubular columns

Sp. #	SHS Column (mm)	SHS Floor (mm)	SHS Ceiling (mm)	Stiff plate (mm)	Axial load (kN)	Tube (#)	$f_y$ (MPa)	$f_u$ (MPa)	$E_s$ (GPa)	$P_{u,Test}$ (kN)	$P_{u,FE}$ (kN)	$\frac{P_{u,Test}}{P_{u,FE}}$	Refs.	
S1	150×150×8	150×250×8	150×150×8	No	286	1	425	575	200	114	120	0.95	[28,29]	
S2	150×150×8	150×250×8	150×150×8	10	286	1	425	575	200	186	165	1.12		
QS1	150×150×8	150×250×8	150×150×8	No	286	1	425	575	200	83	81	1.02		
QS2	150×150×8	150×150×8	150×150×8	10	286	1	425	575	200	120	132	0.91		
QS3	150×150×8	150×250×8	150×150×8	10	286	1	425	575	200	-104	-120	0.86		
QS4	150×150×8	150×250×8	150×150×8	10	143	1	425	575	200	120	132	0.91		
SC1	150×150×8	150×250×8	150×150×8	No	286	2	425	575	200	-139	-125	1.11		
SC2	150×150×8	150×250×8	150×150×8	10	286	2	425	575	200	163	124	1.31		
QSC1	150×150×8	150×250×8	150×150×8	No	286	2	425	575	200	-186	-165	1.12		
QSC2	150×150×8	150×150×8	150×150×8	10	286	2	425	575	200	144	131	1.09		
QSC3	150×150×8	150×250×8	150×150×8	10	286	2	425	575	200	-171	-167	1.02		
QSC4	150×150×8	150×250×8	150×150×8	10	143	2	425	575	200	251	265	0.94		
Mean												<b>1.00</b>		
Cov												<b>0.13</b>		

$f_y, f_u, E_s, P_{u, Test},$  and  $P_{u, FE}$  define yield strength, ultimate strength, elastic modulus, and ultimate resistance via tests and FE

**Table 2** Details and outcomes of axial compression loading on tubular columns

Sp. #	$D/a_c$ (mm)	$B/b_c$ (mm)	$t_c$ (mm)	$L_c$ (mm)	Tube (#)	SHS (types)	$f_{y,w}$ (MPa)	$f_{u,w}$ (MPa)	$E_{s,w}$ (GPa)	$f_{y,C}$ (MPa)	$f_{u,C}$ (MPa)	$E_{s,C}$ (GPa)	$P_{u,Test}$ (kN)	$P_{u,FE}$ (kN)	$\frac{P_{u,Test}}{P_{u,FE}}$	Refs.
AS1	60	60	3	240	1	Square	755	839	209	885	1026	212	615	631	0.97	[57]
AS2	80	80	4	332	1	Square	679	773	199	731	959	210	919	920	1.00	
AS3	80	40	4	238	1	Rectangle	734	817	199	831	962	213	710	704	1.01	
AS4	100	100	4	400	1	Square	586	761	198	811	917	206	1030	1059	0.97	
AS5	60	60	3	2000	1	Square	755	839	209	885	1026	212	162	179	0.91	
AS6	60	60	3	1600	1	Square	755	839	209	885	1026	212	232	224	1.03	
AS7	60	60	3	1200	1	Square	755	839	209	885	1026	212	327	362	0.90	
AS8	60	60	3	800	1	Square	755	839	209	885	1026	212	447	471	0.95	
AS9	80	80	4	1200	1	Square	679	773	199	731	959	210	672	673	1.00	
AS10	80	80	4	2000	1	Square	679	773	199	731	959	210	362	381	0.95	
AS11	80	40	4	1600	1	Rectangle	734	817	199	831	962	213	160	167	0.96	
AS12	80	40	4	1200	1	Rectangle	734	817	199	831	962	213	237	247	0.96	

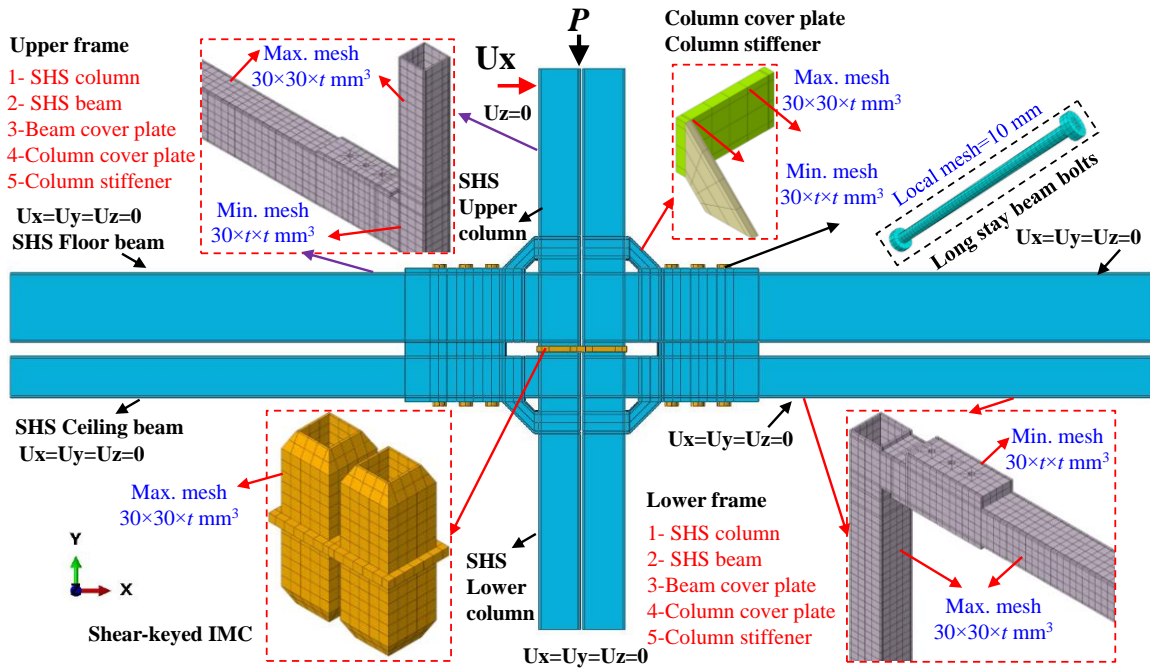
AS13	80	40	4	800	1	Rectangle	734	817	199	831	962	213	367	360	1.02	
AS14	121	76	2	242	1	Elliptical	193	380	676				234	225	1.04	[56]
AS15	121	76	3	242	1	Elliptical	194	420	578				444	443	1.00	
AS16	80	80	3	2815	5	Square	441	521	206				1287	1254	1.03	
AS17	80	80	5	2815	5	Square	403	480	206				1829	1735	1.05	
AS18	100	80	3	2815	5	Rectangle	425	506	206				1495	1407	1.06	
AS19	140	80	4	2815	5	Rectangle	391	522	206				2222	2101	1.06	
AS20	140	80	6	2815	5	Rectangle	359	509	206				2812	2704	1.04	[12–14,58]
AS21	160	80	5	2815	5	Rectangle	403	480	206				3027	2767	1.09	
AS22	200	80	10	2815	5	Rectangle	365	500	206				4805	5105	0.94	
AS23	100	80	3	2815	11	Rectangle	425	506	206				3208	3154	1.02	
AS24	160	80	5	2815	11	Rectangle	403	480	206				6373	6028	1.06	
<b>Mean</b>																<b>1.00</b>
<b>Cov</b>																<b>0.05</b>

$E_{s,w}$ ,  $f_{y,w}$ ,  $f_{u,w}$ ,  $E_{s,c}$ ,  $f_{y,c}$ ,  $f_{u,c}$ ,  $D$ ,  $B$ ,  $L_c$ , and  $t_c$  define the tubes' flat wall and corner regions' elastic modulus, yield strength, ultimate strength, tube's length, width, height, and thickness;  $a_c$  and  $b_c$ , elliptical tube's longest and shortest diameter

**Table 3** Details of compressive resistances of shear-keyed tubes using code prediction equations

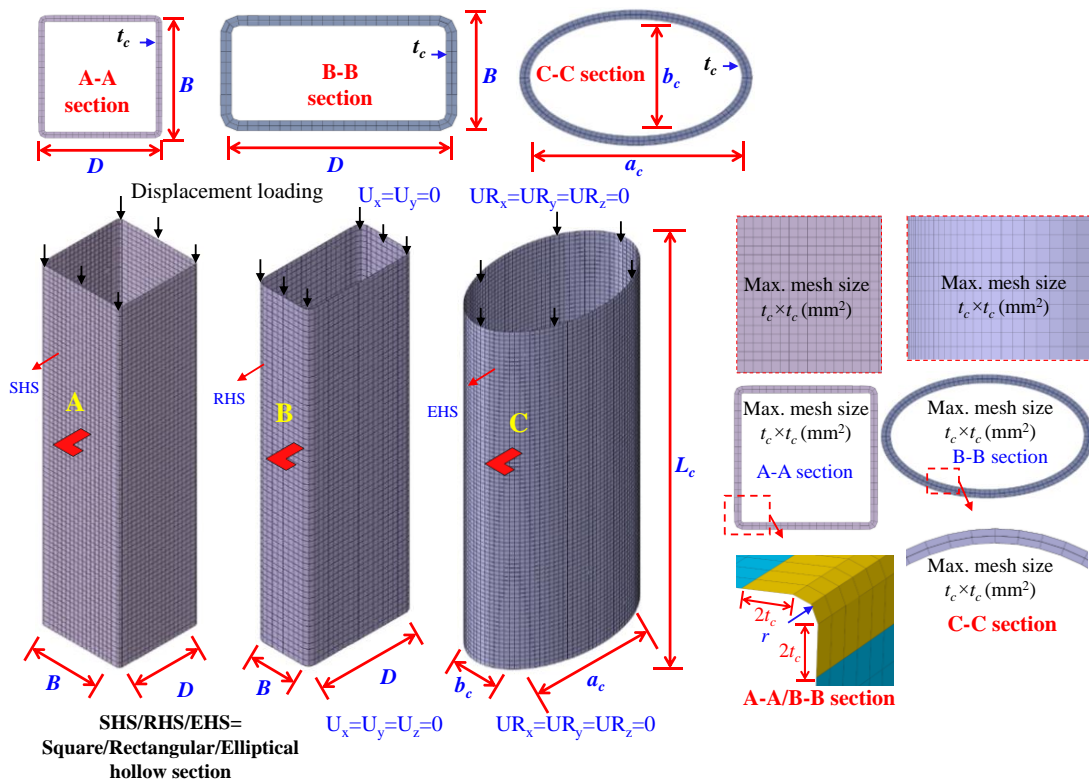
Sp. #	$D$ (mm)	$B$ (mm)	$t_c$ (mm)	$L_c$ (m)	EC3 Class	$P_{u,EC3}$ (kN)	CSA Class	$P_{u,CSA}$ (kN)	AISC Class	$P_{u,AISC}$ (kN)	GB Class	$P_{u,GB}$ (kN)	$f_y$ (MPa)	$P_u$ (kN)
FS-46	200	200	5	3.0	C4	724	C4	645	S	1014	B	1283	380	837
FS-58	200	200	5	1.0	C4	766	C4	676	S	1102	B	1454	380	852
FS-47	200	200	7	3.0	C2	1885	C2	1640	NS	1650	B	1773	380	1523
FS-59	200	200	7	1.0	C2	2065	C2	1836	NS	1825	B	2013	380	1516
FS-60	200	200	8	1.0	C1	2348	C2	2087	NS	2074	B	2289	380	1796
FS-26	200	200	8	1.2	C1	2330	C2	2078	NS	2063	B	2269	380	1781
FS-25	200	200	8	1.5	C1	2303	C2	2060	NS	2041	B	2231	380	2040
FS-27	200	200	8	1.8	C1	2275	C2	2034	NS	2016	B	2192	380	1780
FS-28	200	200	8	2.4	C1	2213	C2	1961	NS	1953	B	2108	380	1778
FS-29	200	200	8	3.0	C1	2141	C2	1862	NS	1874	B	2014	380	1782
FS-30	200	200	8	3.6	C1	2053	C2	1741	NS	1782	B	1905	380	1782
FS-61	200	200	9	1.0	C1	2627	C2	2335	NS	2322	B	2561	380	1948
FS-49	200	200	9	3.0	C1	2394	C2	2080	NS	2095	B	2251	380	1971
FS-70	150	150	10	1.5	C1	2050	C1	1829	NS	1815	C	1876	380	1761
FS-71	180	180	10	1.5	C1	2529	C1	2262	NS	2243	C	2442	380	1807
FS-72	200	200	10	1.5	C1	2847	C1	2546	NS	2524	C	2705	380	1829
FS-73	220	220	10	1.5	C1	3164	C2	2827	NS	2805	B	3037	380	1841
FS-74	250	250	10	1.5	C1	3641	C3	3247	NS	3224	B	3544	380	1903
FS-85	160	80	8	1.5	C1	1310	C1	1006	NS	1032	C	1103	380	1220
FS-86	200	120	8	1.5	C1	1751	C2	1551	NS	1544	B	1667	380	1498
FS-87	220	140	8	1.5	C2	2014	C3	1796	NS	1783	B	1932	380	1635
FS-88	250	180	8	1.5	C3	2472	C3	2211	NS	2192	B	2390	380	1855

$P_{u,EC3}$ ,  $P_{u,CSA}$ ,  $P_{u,AISC}$ ,  $P_{u,GB}$ ,  $P_u$ , and Cov define ultimate compressive resistance via EC3:1-1, CSA S16, AISC360-16, GB50017, FEA, and coefficient of variation



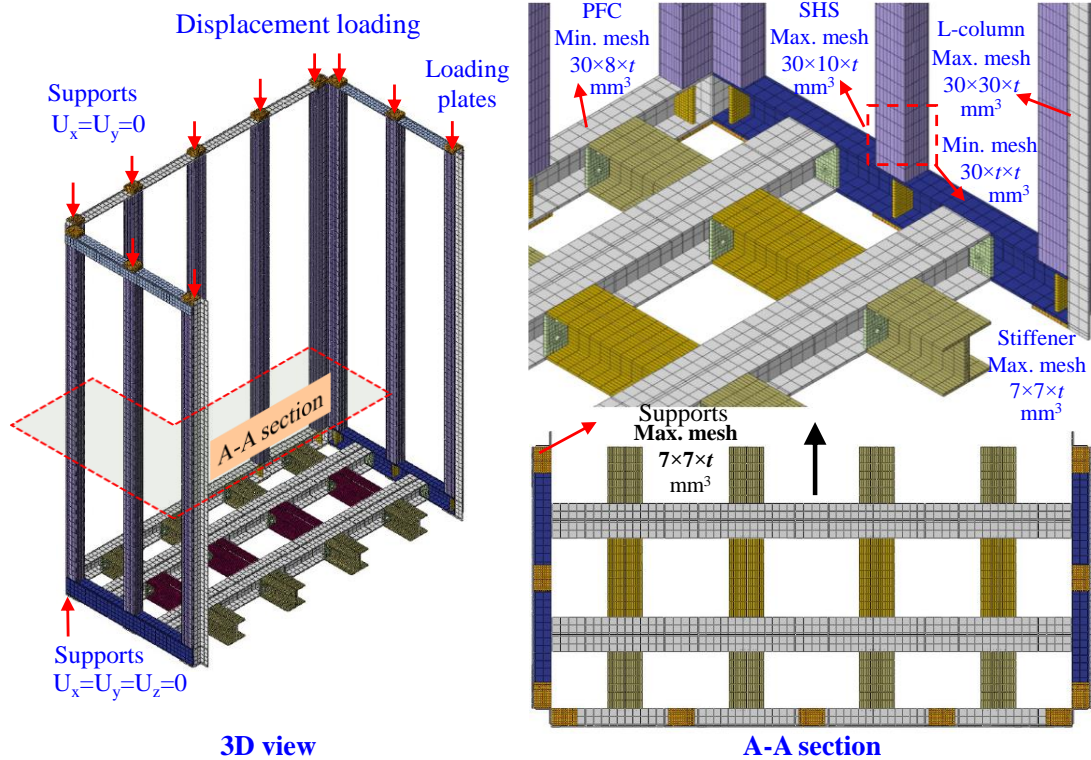
121

Fig. 2 FEM details of a shear-keyed frame by Chen et al. [28,29]



122  
123

Fig. 3 FEM details of tubes by Theofanous and Gardner [57]



124

3D view

125

**Fig. 4** FEM details of tubular walls by Hou et al. [58] and Khan et al. [12,13]

126

### 3 Nonlinear finite element modeling

127

The cited tests' findings in section 2 are used to build a reliable FEM of the shear-keyed

128

tube to analyze the parametric effect.

129

#### 3.1 Generalized finite element model

130

The modeling and finite element analysis (FEA) were performed using ABAQUS [59].

131

ABAQUS/Static general solver was used for the validation of tests carried out on shear-

132

keyed frames by Chen et al. [28,29]. Moreover, tests conducted by Theofanous and

133

Gardner [56,57], Hou et al. [58], and Khan et al. [12,13] were validated using buckling

134

and post-buckling analyses. Elastic buckling was performed with ABAQUS/Linear

135

perturbation buckle-type solver using the subspace iteration method to determine the

136

buckling loads and modes. Then ABAQUS/static Riks-type solver, a variant of the

137

classical arc-length method, was adopted to determine the load-shortening and failure

138

mechanism in the nonlinear analysis.

139

As depicted in **Fig. 2** and **Table 1**, the cover plates, stiffeners, beams, and columns

140

were treated as single-frame components in the FEM of the shear-keyed frame. Bolt

141 heads, shafts, and nuts were modeled without threads and without considering the bolt-  
142 to-hole gap. The FEM of cold-formed stainless-steel tubes is shown in **Fig. 3**, and that  
143 of hot-rolled tubular column walls is depicted in **Fig. 4**. Their structural members  
144 preserve **Table 2** dimensions. These FEMs modeled varying shape tubes, cover plates,  
145 stiffeners, beam bolts, angle columns, floor channels, angle ceiling beams, connecting  
146 plates with holes, and the floor chassis. This improves simulation accuracy, ensuring  
147 simulation on shear-keyed tubes' ultimate strength.

### 148 **3.2 Constraints, loadings, interactions, and geometric imperfections**

149 Following shear-keyed frames in [28,29], the lower columns' movement was restricted  
150 in all directions. The upper columns' were free with lateral displacement and axial  
151 loading applied in the vertical direction. There were constraints on beams in the vertical  
152 direction. Moreover, beams' and columns' out-of-plane movement and rotation were  
153 constrained, allowing them to rotate in-plane. Loading and boundary conditions on  
154 columns and beams were attained by defining the reference nodes on the cross-sections'  
155 midpoint with surface-based coupling constraints that limit the translation and rotation  
156 at the coupling nodes. Using the "penalty friction formulation," the contact between  
157 beams and bolts, neighboring columns and beams, and the column and the shear key  
158 was simulated as surface-to-surface contact (standard), with "hard contact" as the  
159 normal behavior and "finite sliding" as the tangential behavior. The friction coefficient  
160 used for penalty friction formulation was 0.3.

161 Following the experimental setup in [56,57], all degrees of freedom were restrained at  
162 the stub column cross-section ends, except for vertical translation for top-end nodes, to  
163 simulate displacement loading and allow vertical shortening. Similar constraints were  
164 applied to the flexural buckling FEMs of long tubes, except for the unrestrained  
165 rotational degree of freedom about the buckling axis, allowing pin-ended boundaries.

166 Surface-based coupling constraints were achieved to apply loads or boundary  
167 conditions to tube ends using kinematic coupling. The motion of a collection of (slave)  
168 nodes on end surfaces was coupled to the rigid body motion defined by the reference  
169 node on cross-sectional centers. Kinematic couplings were introduced by constraining  
170 the rotational and translational degrees of freedom at the coupling nodes. The  
171 membrane residual stresses due to seam-welding have a negligible effect on the  
172 ultimate capacity of stainless SHS. The residual stresses caused by the bending residual  
173 stresses are inherent in the material stress-strain properties. Consequently, residual  
174 stresses are not explicitly introduced into the FEMs [43,57,60,61]. Simulating  
175 geometric imperfections involved examining buckling shapes and comparing load-  
176 shortening curves from Refs. [56,57]. Initially, the eigenmode analysis obtained several  
177 buckling modes, followed by the nonlinear Riks analysis and selecting the closest  
178 buckling mode with test failure mode for applying geometric imperfections. Local  
179 geometric imperfections were applied to stubs, whereas local and global imperfections  
180 as eccentricity were applied to long columns. It was discovered that the failure mode of  
181 most test specimens, i.e., stubs or long tubes, was limited to the lowest buckling mode,  
182 i.e., the first buckling mode, consistent with test sources in Refs. [56,57]. According to  
183 Ref. [57], the study chose the local imperfection of  $t_c/100$  and the global imperfection  
184 magnitude of  $L_c/1500$ .

185 Moreover, the motion of the top and bottom beams was restrained in hot-rolled tubular  
186 walls in all directions as Refs. [58] and [12,13]. In contrast, the bottom portion vertical  
187 movement and rotations were released to allow specimen shortening. In order to apply  
188 displacement loading and boundary conditions, surface-based kinematic coupling  
189 constraints were achieved by defining the reference nodes on cushion block centers  
190 above and below the ceiling and floor beams and restricting the rotational and

191 translational degrees of freedom at the coupling nodes. Beams have been welded to  
192 cushion blocks, columns, and angles. Moreover, modular floors included welded floors  
193 and stringer beams; thus, the "tie constraint" with surface-to-surface contact was used,  
194 preventing their relative movement. Wall failure was not restricted to strength failure;  
195 it was caused by global instability beginning with the global buckling of the middle  
196 column of the front walls and the outer columns of the exterior sidewall columns as  
197 determined by Hou et al. [58] and Khan et al. [12,13]. Moreover, while using advanced  
198 analysis, member and frame imperfections are suggested to be modeled with a  
199 minimum value of  $L_c/500$  and a maximum of  $L_c/1000$ , which are considerably larger  
200 and incorporate members' local geometric imperfections [62]. Therefore, buckling  
201 analysis considered the global instability mode and neglected local imperfections, as  
202 reported in Refs. [63,64] and [10]. The load and ultimate end-shortening appear to be  
203 better anticipated using the magnitude of  $L_c/600$ , which was incorporated into the FEM.  
204 This value of imperfection was obtained by comparing the load-shortening findings to  
205 those of test load-shortening curves.

### 206 **3.3 Elements type and mesh sizes**

207 The shear-keyed frame utilized hexagonally structured mesh controls with an eight-  
208 node linear brick, reduced integration, and Hourglass Control Element Type (C3D8R).  
209 Corners, edges, bolts, and holes have finely meshed with minimal mesh density, as  
210 shown in **Fig. 2**. Still, other regions utilized the maximum mesh sizes. It was discovered  
211 that  $30 \times 30 \times t$ ,  $30 \times t \times t$ , and 10 mm were feasible mesh sizes for the upper and lower  
212 frame skeletons, shear-keyed IMC, cover plates, stiffeners, and beam bolts. Four-noded  
213 double-curved shell elements (S4R) were employed to discretize cold-formed thin-  
214 walled stainless steel tube sections, as shown in **Fig. 3**. All models used element sizes  
215 equal to the material thickness for corners and flat surfaces. Regarding corners, they

216 have partitioned at a distance of  $2t_c$  times from the edges of curved regions' root radii  
217 ( $r$ ), assuming their geometry approximates circular arcs. The  $r$  values of tubes are  
218 computed from the source study Refs. [56,57]. Connecting plates with holes in walls  
219 used advanced hexagonal sweep mesh controls, whereas remaining deformable solid  
220 parts adopted the structured C3D8R element type. The feasible mesh sizes for SHS  
221 tubes, angle columns, stiffeners, connecting plates, PFC floor beams, and cushion  
222 blocks were determined to be  $30 \times 10 \times t$ ,  $30 \times 30 \times t$ ,  $30 \times 8 \times t$ , and  $7 \times 7 \times t$ , following Refs.  
223 [58] and [12,13], as displayed in **Fig. 4**. Stress singularity can be caused by mesh  
224 convergence, point loads, boundary conditions applied to point supports, sharp corners,  
225 small radius on corners, contact on sharp corners, fixed boundary conditions, and effect  
226 of local disturbances [65–72]. However, it does not affect displacement, deformation,  
227 and stress elsewhere as St. Venant's principle; thus, it was ignored [65–67,70,71].

### 228 **3.4 Material simulation**

229 The hot-rolled shear-keyed frames and multi-column walls neglect tube corner  
230 strengthening and root radii, as shown in **Figs. 2 and 4**. Moreover, the cold-forming  
231 method produces increased strength in the corner regions; thus, the enhanced strength  
232 was applied to corners that extended  $2t_c$  beyond the curved corner regions into the flat  
233 portions of the stainless steel cross-section, as depicted in **Fig. 3** [56,57]. The corner  
234 material properties were applied to the corner and the neighboring flat regions up to  $2t_c$ .  
235 In contrast, flat wall properties were assigned to the remaining areas of the cross-section  
236 as per the techniques followed in Refs. [56,57] and [73–75]. The material properties  
237 essential for material definition in the FEM development and validation are listed in  
238 **Tables 1 and 2**. **Table 2** lists the material properties of the flat regions and the corner  
239 region from the corner to the flat sections by a distance of  $2t_c$ . As per C.6 of EN 1993-

240 1-5:2006 (E) [76], engineering stress-strain values can be converted into true ones using  
241 Eqns. (1) and (2). The chosen Poisson ratio is 0.3.

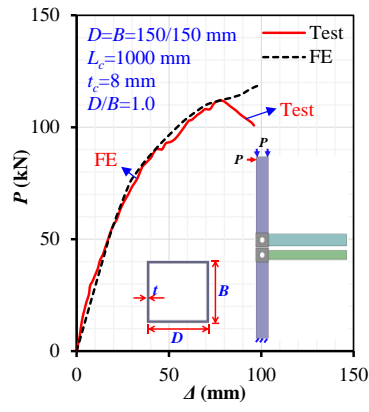
$$\sigma_T = \sigma_E(1 + \varepsilon_E) \quad (1)$$

$$\varepsilon_T = \ln(1 + \varepsilon_E) \quad (2)$$

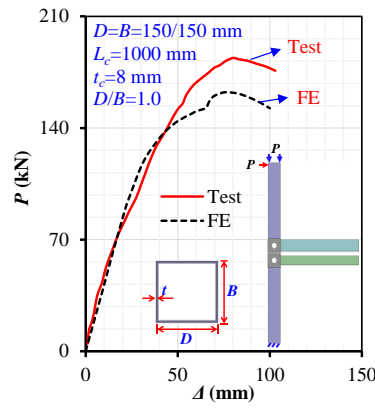
242 where  $\sigma_E/\varepsilon_E$  are Engineering stress/strain while  $\sigma_T/\varepsilon_T$  True stress/strain.

### 243 3.5 Validations

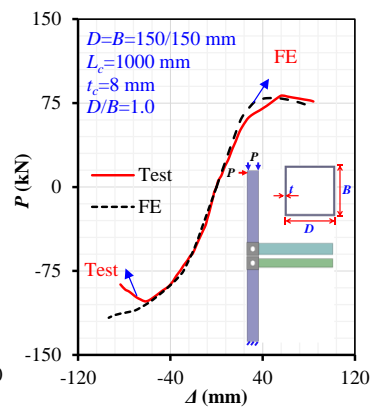
244 **Figure 5(a-ac) and Tables 1 and 2** compare FE and experimental load-shortening  
245 curves and test-to-prediction ratios, indicating FEMs predict shortening behavior  
246 accurately with minor differences in stiffness or post-ultimate recession. These  
247 deviations were induced by soft support, material models, modeling simplifications,  
248 and insufficient geometric imperfection simulations. According to the test-to-FE  
249 prediction ratios in **Table 1**, the FE's average estimations for 12 tests were 1.0 with a  
250 Cov of 0.13. Similarly, **Table 2** shows that the FE's average assessments for 24 tests  
251 were 1.0 with a Cov of 0.05, indicating minor prediction errors for  $P_u$ . **Figure 6**  
252 compares FEA-deformed shapes to experimental results, showing FEM can accurately  
253 anticipate failure behavior. For instance, columns gap widening, columns and beams  
254 fracture, local inward and outward buckling (IB and OB), global buckling (GB),  
255 stiffener bending, channel beam extrusion, angle weld fracture, and restraint effect. This  
256 ensures that the developed FEM could predict columns' axial compression behaviors at  
257 both the member and structural levels.



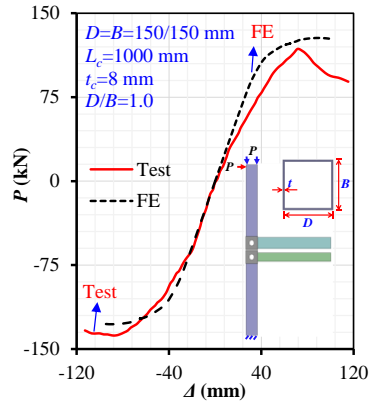
a) S1



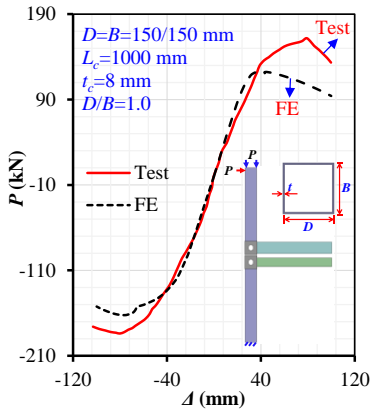
b) S2



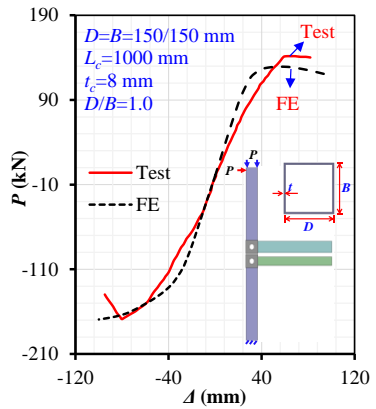
c) QS1



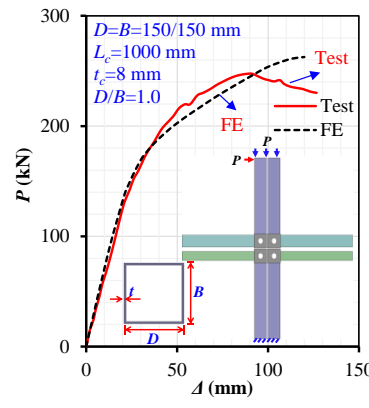
d) QS2



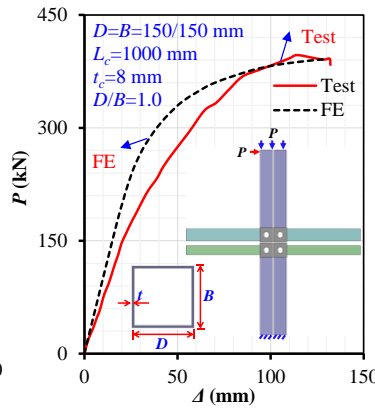
e) QS3



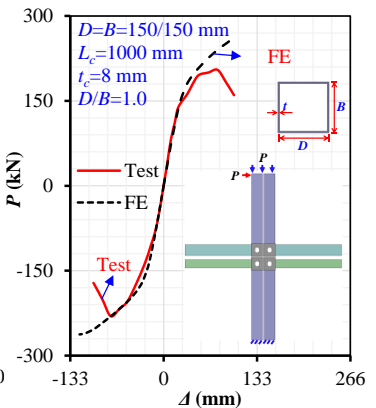
f) QS4



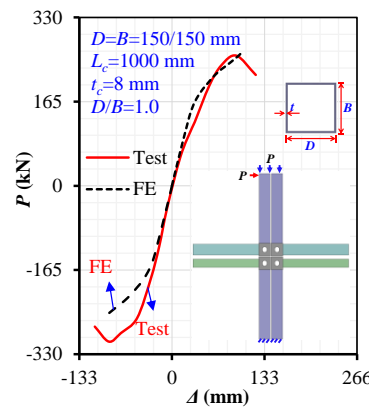
g) SC1



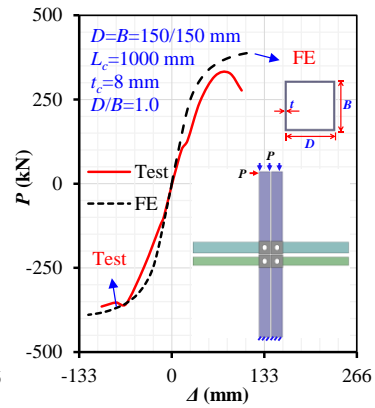
h) SC2



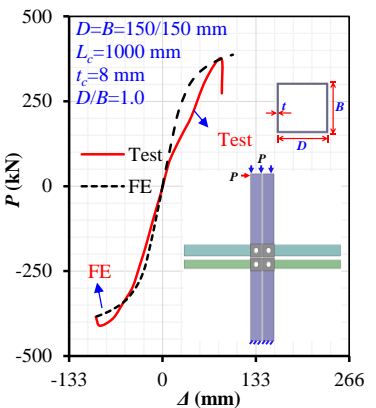
i) QSC1



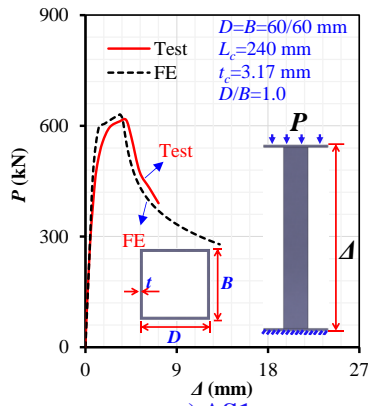
j) QSC2



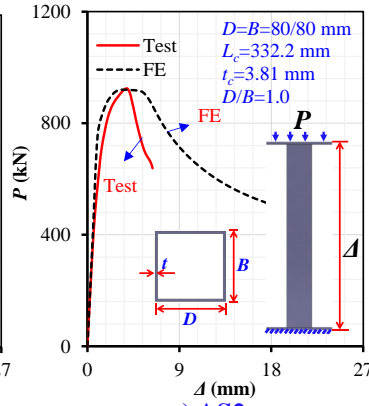
k) QSC3



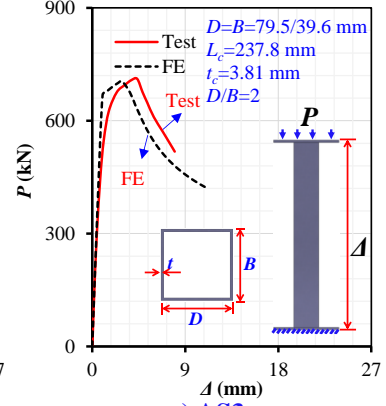
l) QSC4



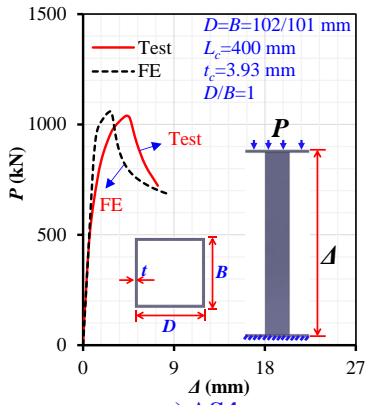
m) AS1



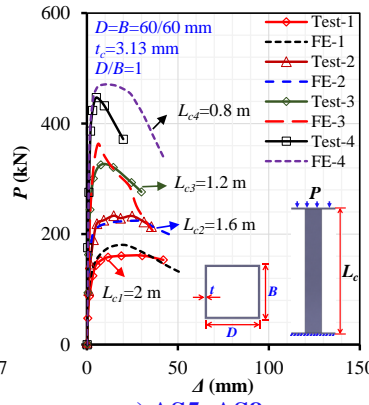
n) AS2



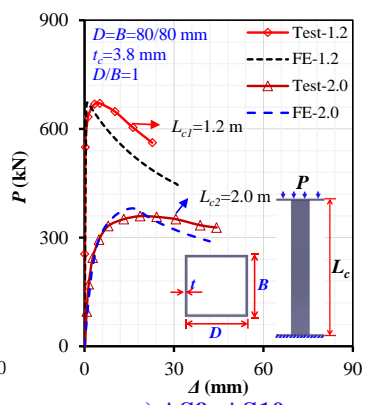
o) AS3



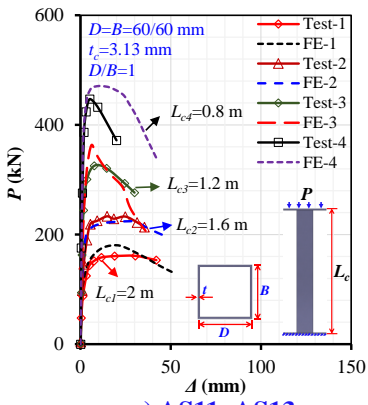
p) AS4



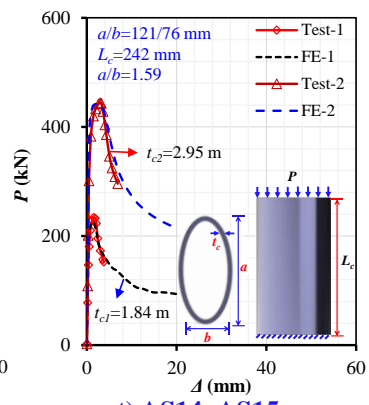
q) AS5~AS8



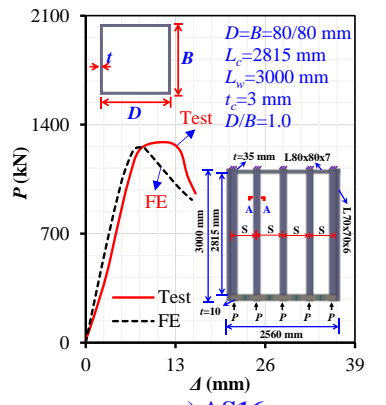
r) AS9~AS10



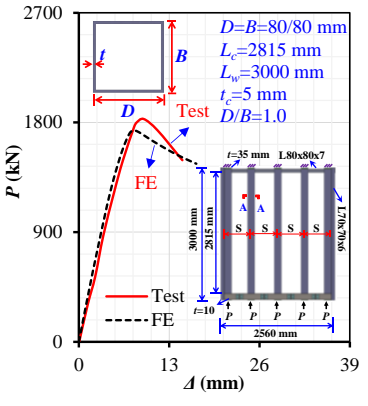
s) AS11~AS13



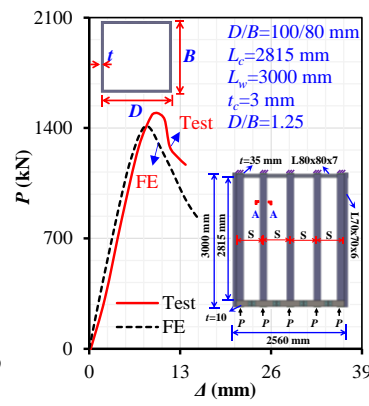
t) AS14~AS15



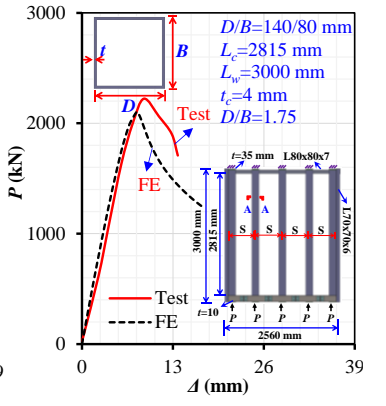
u) AS16



v) AS17



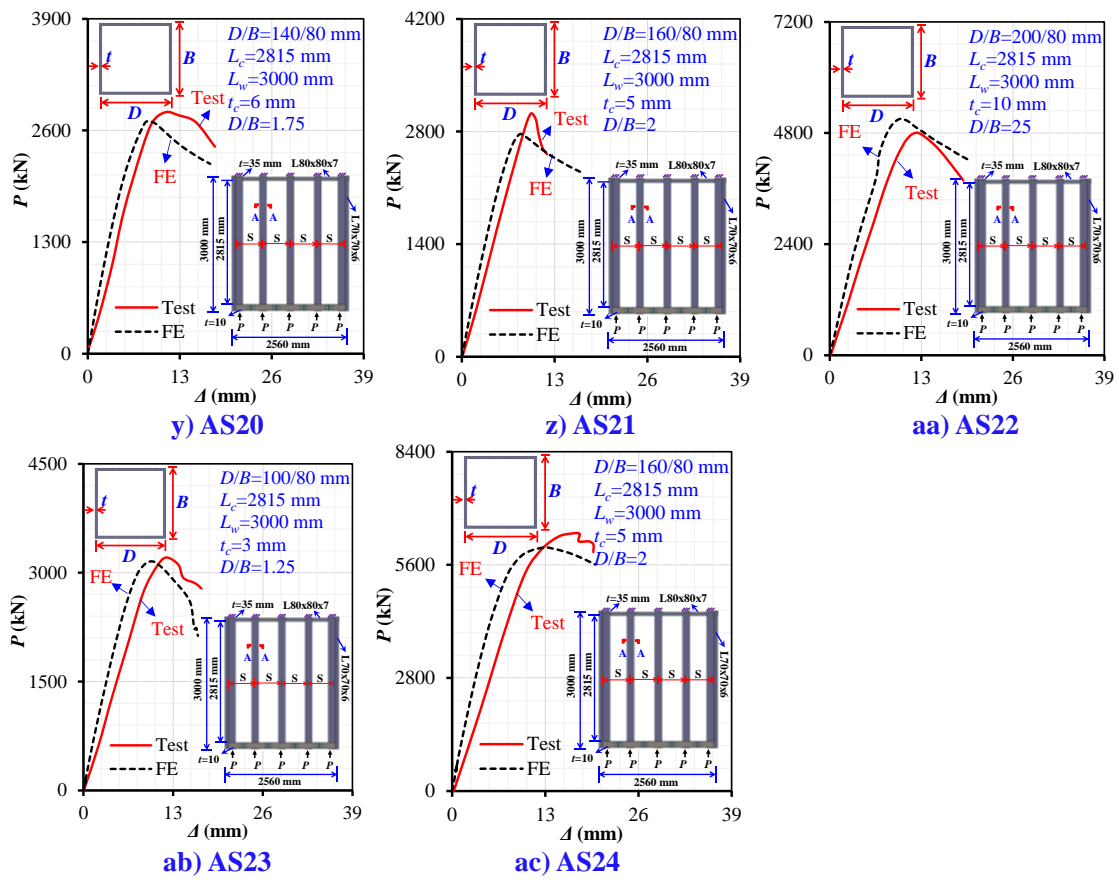
w) AS18



x) AS19

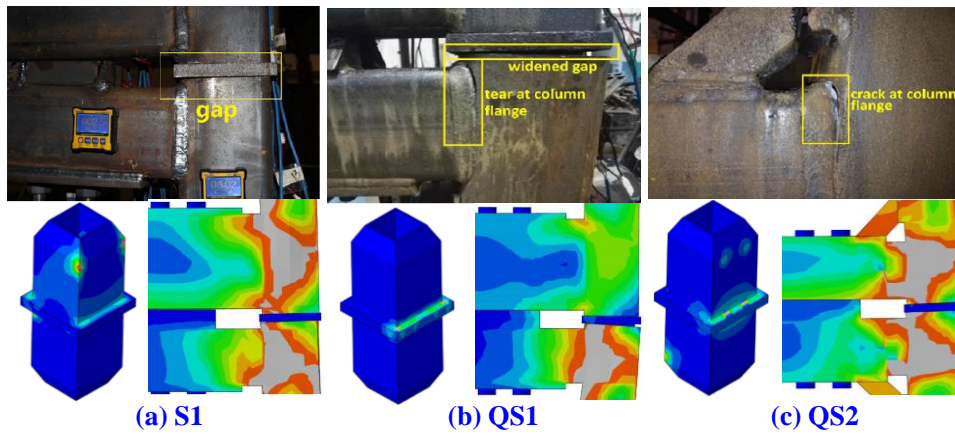
259  
260  
261

262  
263

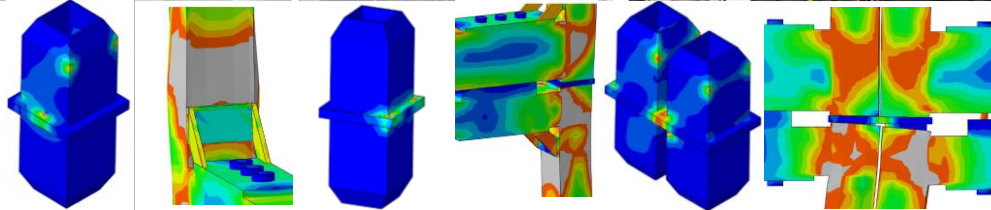
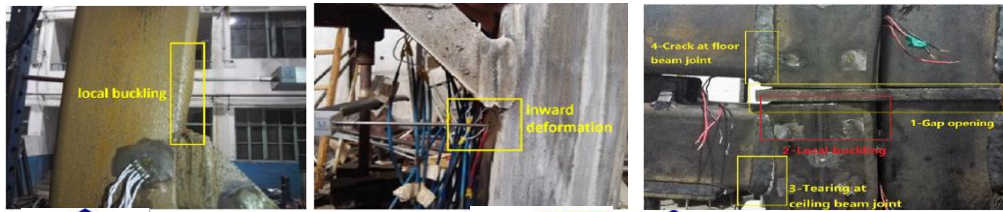


264  
265

Fig. 5 Test to FE-predictions comparison



266

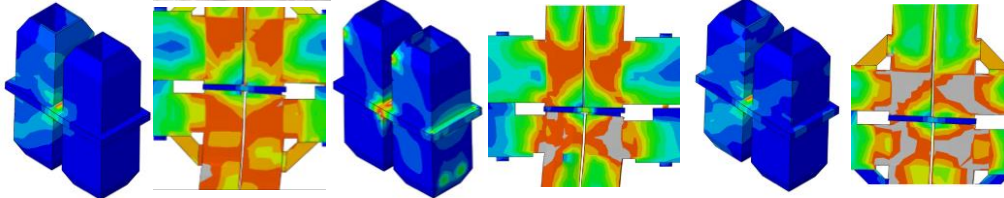


267

(d) QS3

(e) QS4

(f) SC1

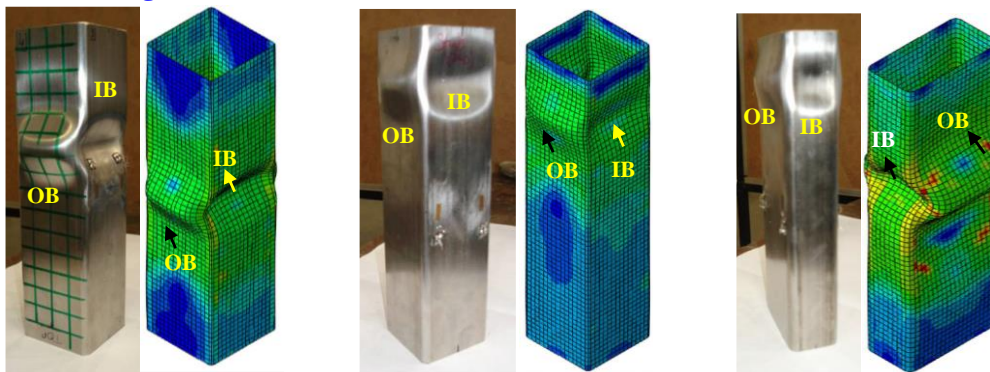


268

(g) SC2

(h) QSC1

(i) QSC2

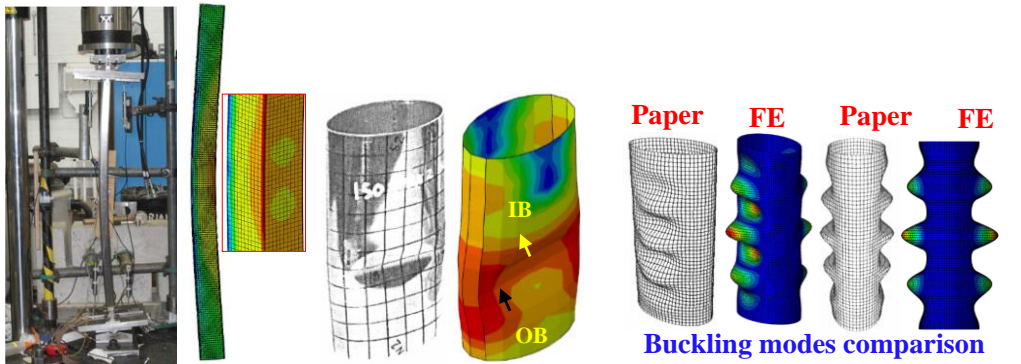


269

(j) 60×60×3

(k) 80×80×4

(l) 80×40×4



270

(m) 80×40×4-1600

(n) 121×76×2

**Buckling modes comparison**  
 Paper FE Paper FE  
 (o) Elliptical SHS buckling mode

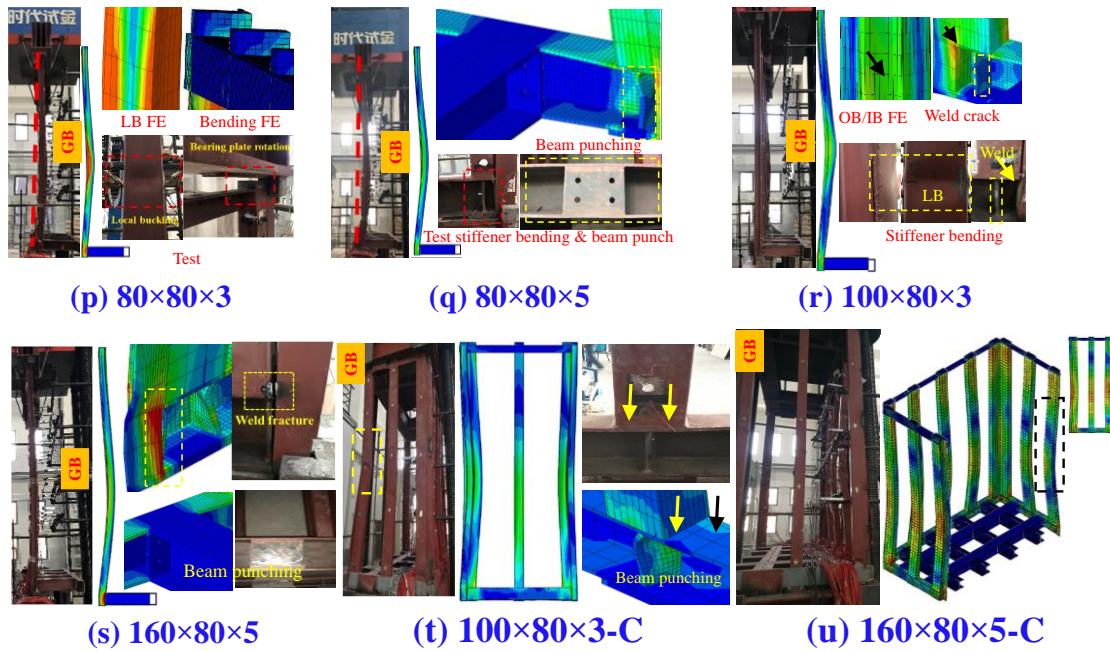


Fig. 6 Test to FE-failures comparison

#### 4 Numerical studies on shear-keyed tubes in MSS

##### 4.1 Investigated parameters and behavior details

A parametric study employing 108 validated FEMs investigated the effects of initial imperfection, shear-key height ( $L_t$ ), thickness ( $t_t$ ), steel tube height ( $L_c$ ), width ( $B$ ), length ( $D$ ), and thickness ( $t_c$ ) on the compressive behavior of shear-keyed tubes. These FEMs are categorized by varying  $t_t$  (15, 20, and 25 mm for given  $L_t$  of 100, 150, and 250 mm),  $L_t$  (75, 150, 250, and 300 mm with 15, 20, 25, and 35 mm  $t_t$ ),  $L_c$  (1.2, 1.8, 2.4, 3.0 and 3.6 m for given  $L_t$  of 75, 150, 250, and 300 mm),  $t_c$  (5, 7, 8, and 9 mm with 1 and 3 m  $L_c$ , and for given  $L_t$  of 100, 150, and 250 mm),  $D/B$  (150/150, 180/180, 200/200, 220/220, 250/250, 160/80, 200/120, 220/140, and 250/180 mm for given  $L_t$  of 100, 150, and 250 mm), and imperfections ( $t_c/100$ ,  $t_c/10$ ,  $t_c/5$ ,  $t_c/2$ ,  $t_c$ ,  $L_c/2000$ ,  $L_c/1500$ ,  $L_c/1000$ ,  $L_c/500$ ,  $D/20$ ,  $D/8$ , and  $D/4$ ). **Table 4** lists further information about these studies.

The behavior compares the ultimate compressive resistance ( $P_u$ ), axial shortening ( $\Delta_u$ ), initial stiffness ( $K_e$ ), and ductility index ( $DI$ ) of shear-keyed tubes. The load-shortening curves of shear-keyed tubes can be used to determine the  $P_u$  and  $\Delta_u$ . Moreover, it is possible to calculate the  $K_e$  using Eqn. 3. Similarly,  $DI$  can be calculated by Eqn. 4. Pre-

289 and post-ultimate ductility of the shear-keyed tubes are represented by  $\Delta_u$  and  $DI$ . **Table**

290 **4** lists each FEM's  $P_u$ ,  $\Delta_u$ ,  $K_e$ , and  $DI$  values [77].

$$K_e = P_{45\%} / \Delta_{45\%} \quad (3)$$

$$DI = \Delta_{85\%} / \Delta_u \quad (4)$$

291 where  $P_{45\%}$ ,  $\Delta_{45\%}$  and  $\Delta_{85\%}$  represent  $0.45P_u$  and shortening at  $P_{45\%}$  and  $P_{85\%}$ .

292 **Figure 8(b)** shows the computation procedure for these terminologies [78].

**Table 4** Detailed parametric results of shear-keyed tubes

Item	$D$ (mm)	$B$ (mm)	$t_c$ (mm)	$t_t$ (mm)	$d$ (mm)	$b$ (mm)	$L_c$ (mm)	$L_t$ (mm)	$P_u$ (kN)	$K_e$ (kN/mm)	$\Delta_u$ (mm)	$DI$ Ratio
No Key	200	200	8	-	-	-	1500	-	2398	704	7.9	2.5
FS-1	200	200	8	15	180	180	1500	100	1346	471	16.4	2.9
FS-2	200	200	8	20	180	180	1500	100	1490	538	14.9	3.4
FS-3	200	200	8	25	180	180	1500	100	2031	623	10.8	2.5
FS-4	200	200	8	15	180	180	1500	150	1397	496	13.7	2.2
FS-5	200	200	8	20	180	180	1500	150	1518	570	14.9	2.0
FS-6	200	200	8	25	180	180	1500	150	1807	733	7.8	3.5
FS-7	200	200	8	15	180	180	1500	250	1657	572	9.9	3.3
FS-8	200	200	8	20	180	180	1500	250	1786	610	9.1	2.8
FS-9	200	200	8	25	180	180	1500	250	2099	659	9.8	2.4
FS-10	200	200	8	15	180	180	1500	75	1397	495	12.9	2.4
FS-11	200	200	8	15	180	180	1500	150	1397	496	13.7	2.2
FS-12	200	200	8	15	180	180	1500	250	1396	501	11.5	2.6
FS-13	200	200	8	15	180	180	1500	300	1397	501	13.0	2.3
FS-14	200	200	8	20	180	180	1500	75	1518	562	14.4	2.1
FS-15	200	200	8	20	180	180	1500	150	1518	570	14.9	2.0
FS-16	200	200	8	20	180	180	1500	250	1521	578	11.9	2.2
FS-17	200	200	8	20	180	180	1500	300	1523	590	9.6	2.5
FS-18	200	200	8	25	180	180	1500	75	1781	719	8.0	2.0
FS-19	200	200	8	25	180	180	1500	150	1807	733	7.8	3.5
FS-20	200	200	8	25	180	180	1500	250	1872	735	6.2	2.1
FS-21	200	200	8	25	180	180	1500	300	1875	736	6.7	2.1
FS-22	200	200	8	35	180	180	1500	75	1986	768	4.0	1.6
FS-23	200	200	8	35	180	180	1500	150	2030	790	4.2	2.9
FS-24	200	200	8	35	180	180	1500	250	2040	764	5.3	2.2
FS-25	200	200	8	35	180	180	1500	300	2040	787	6.7	1.6
FS-26	200	200	8	25	180	180	1200	75	1781	873	7.8	3.2
FS-27	200	200	8	25	180	180	1800	75	1780	618	7.3	2.2
FS-28	200	200	8	25	180	180	2400	75	1778	495	6.1	2.4
FS-29	200	200	8	25	180	180	3000	75	1782	404	7.1	2.2
FS-30	200	200	8	25	180	180	3600	75	1782	339	8.2	2.0
FS-31	200	200	8	25	180	180	1200	150	1806	883	8.0	2.2
FS-32	200	200	8	25	180	180	1800	150	1807	635	7.2	2.2
FS-33	200	200	8	25	180	180	2400	150	1806	487	7.2	2.3
FS-34	200	200	8	25	180	180	3000	150	1809	398	8.3	2.0
FS-35	200	200	8	25	180	180	3600	150	1807	340	7.8	2.2
FS-36	200	200	8	25	180	180	1200	250	1858	891	6.4	2.2
FS-37	200	200	8	25	180	180	1800	250	1875	628	6.9	1.9
FS-38	200	200	8	25	180	180	2400	250	1873	490	6.6	1.9
FS-39	200	200	8	25	180	180	3000	250	1876	405	6.7	1.9
FS-40	200	200	8	25	180	180	3600	250	1875	339	8.0	1.7
FS-41	200	200	8	25	180	180	1200	300	1859	891	5.7	2.7
FS-42	200	200	8	25	180	180	1800	300	1879	643	5.6	2.3
FS-43	200	200	8	25	180	180	2400	300	1877	498	5.7	2.4
FS-44	200	200	8	25	180	180	3000	300	1880	401	7.3	2.0
FS-45	200	200	8	25	180	180	3600	300	1880	340	7.7	2.0
FS-46	200	200	5	25	180	180	3000	100	837	136	14.3	1.4

FS-47	200	200	7	25	180	180	3000	100	1523	336	7.8	1.6
FS-48	200	200	8	25	180	180	3000	100	1800	399	8.5	1.8
FS-49	200	200	9	25	180	180	3000	100	1971	418	15.0	1.7
FS-50	200	200	5	25	180	180	3000	150	838	137	13.9	2.1
FS-51	200	200	7	25	180	180	3000	150	1537	329	8.0	1.4
FS-52	200	200	8	25	180	180	3000	150	1809	398	8.3	2.0
FS-53	200	200	9	25	180	180	3000	150	1971	422	12.9	1.8
FS-54	200	200	5	25	180	180	3000	250	837	137	13.4	1.5
FS-55	200	200	7	25	180	180	3000	250	1606	342	8.4	1.5
FS-56	200	200	8	25	180	180	3000	250	1876	405	6.7	1.9
FS-57	200	200	9	25	180	180	3000	250	1998	425	13.5	1.8
FS-58	200	200	5	25	180	180	1000	100	852	445	4.6	2.5
FS-59	200	200	7	25	180	180	1000	100	1516	755	7.5	2.2
FS-60	200	200	8	25	180	180	1000	100	1796	1017	8.4	3.0
FS-61	200	200	9	25	180	180	1000	100	1948	1098	8.3	2.7
FS-62	200	200	5	25	180	180	1000	150	850	445	4.9	2.4
FS-63	200	200	7	25	180	180	1000	150	1524	755	7.2	1.5
FS-64	200	200	8	25	180	180	1000	150	1798	1018	7.7	3.7
FS-65	200	200	9	25	180	180	1000	150	1950	1103	10.0	2.2
FS-66	200	200	5	25	180	180	1000	250	851	445	4.8	2.4
FS-67	200	200	7	25	180	180	1000	250	1561	753	7.0	1.7
FS-68	200	200	8	25	180	180	1000	250	1834	1029	5.3	2.8
FS-69	200	200	9	25	180	180	1000	250	1965	1150	5.8	3.1
FS-70	150	150	10	25	130	130	1500	100	1761	540	13.3	3.0
FS-71	180	180	10	25	160	160	1500	100	1807	688	14.9	3.2
FS-72	200	200	10	25	180	180	1500	100	1829	817	8.9	4.3
FS-73	220	220	10	25	200	200	1500	100	1841	823	9.9	4.2
FS-74	250	250	10	25	230	230	1500	100	1903	961	6.9	5.3
FS-75	150	150	10	25	130	130	1500	150	1762	637	16.2	3.0
FS-76	180	180	10	25	160	160	1500	150	1807	691	15.4	3.4
FS-77	200	200	10	25	180	180	1500	150	1828	821	9.3	5.0
FS-78	220	220	10	25	200	200	1500	150	1841	843	9.7	5.0
FS-79	250	250	10	25	230	230	1500	150	1903	967	7.1	7.2
FS-80	150	150	10	25	130	130	1500	250	1769	653	14.2	4.5
FS-81	180	180	10	25	160	160	1500	250	1811	719	13.4	4.0
FS-82	200	200	10	25	180	180	1500	250	1836	851	8.1	4.6
FS-83	220	220	10	25	200	200	1500	250	1849	1006	9.9	5.6
FS-84	250	250	10	25	230	230	1500	250	1899	994	7.2	8.0
FS-85	160	80	8	25	140	60	1500	100	1220	466	6.4	3.0
FS-86	200	120	8	25	180	100	1500	100	1498	608	6.1	3.2
FS-87	220	140	8	25	200	120	1500	100	1635	675	8.6	2.5
FS-88	250	180	8	25	230	160	1500	100	1855	792	8.3	3.4
FS-89	160	80	8	25	140	60	1500	150	1220	464	7.1	2.8
FS-90	200	120	8	25	180	100	1500	150	1498	607	6.4	2.9
FS-91	220	140	8	25	200	120	1500	150	1635	686	6.4	2.9
FS-92	250	180	8	25	230	160	1500	150	1862	808	6.9	2.6
FS-93	160	80	8	25	140	60	1500	250	1209	469	6.1	2.5
FS-94	200	120	8	25	180	100	1500	250	1513	609	6.4	2.3
FS-95	220	140	8	25	200	120	1500	250	1651	685	7.9	4.1
FS-96	250	180	8	25	230	160	1500	250	1889	791	7.0	4.7
FS-97-t/100	200	200	8	25	180	180	1500	150	1991	834	3.2	5.1
FS-98-t/10	200	200	8	25	180	180	1500	150	1916	813	4.9	4.3
FS-99-t/5	200	200	8	25	180	180	1500	150	1860	771	7.8	3.1
FS-100-t/2	200	200	8	25	180	180	1500	150	1736	658	10.8	3.0
FS-101-t	200	200	8	25	180	180	1500	150	1594	524	15.7	2.2
FS-102-L/2000	200	200	8	25	180	180	1500	150	1920	815	5.2	2.5
FS-103-L/1500	200	200	8	25	180	180	1500	150	1901	803	5.3	4.0
FS-104-L/1000	200	200	8	25	180	180	1500	150	1867	776	7.1	2.1
FS-105-L/500	200	200	8	25	180	180	1500	150	1780	707	8.7	3.1
FS-106-D/20	200	200	8	25	180	180	1500	150	1808	733	8.4	2.1
FS-107-D/8	200	200	8	25	180	180	1500	150	1808	733	8.4	2.1
FS-108-D/4	200	200	8	25	180	180	1500	150	1808	733	8.4	2.1

$t_t$ ,  $L_t$ ,  $d$ ,  $b$ ,  $P_u$ ,  $\Delta_u$ ,  $K_e$ , and  $DI$  denote shear keys' thickness, height, length, width, tube's ultimate compressive

resistance, axial shortening, initial stiffness, and ductility index, respectively.

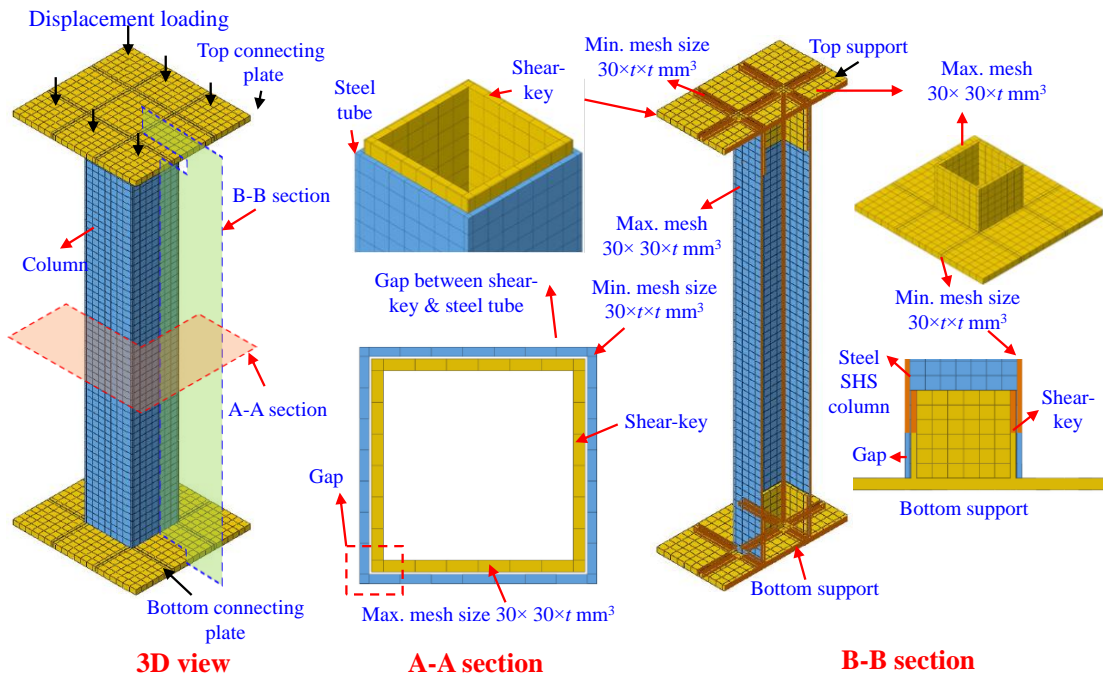
## 293 **4.2 Tubes design**

294 As depicted in Figs. 1(a) and 7, the shear-keyed tube design was based on the authors'  
295 five-story corner-supported MSS office buildings designed under Chinese steel design  
296 code GB 50017-2017 [79]. The Haoshi office building was constructed with 68 modular  
297 units measuring  $13.8 \times 3.6 \times 3.5$  and  $14.4 \times 3.6 \times 3.5$  m. In contrast, two blocks of the  
298 Tianjin Ziya office building utilized 314 modules measuring  $8.5 \times 3.0 \times 3.0$  and  
299  $6.7 \times 3.0 \times 3.0$  m. Additionally, each of these hybrid types of MSS consisted of two steel  
300 frame cores functioning as staircases to prevent lateral sway and IMC rotation,  
301 improving the buckling strength of columns [80]. The primary objective was to conduct  
302 extensive parametric and analytic studies; consequently, tube cross-sections were  
303 selected per the prototype project. The inflection point was established by designing the  
304 column height as half of the actual, as indicated in **Fig. 1(b)**, and tube height was  
305 designed using column subassembly, as recommended in Ref. [81]. In this investigation,  
306 the top and lower plates were connected by a box-shaped shear key [26]. Shear keys  
307 were inserted inside SHS tubes to replicate the actual scenario, and connecting plates  
308 were not welded to the tubes to allow movement. In order to account for fabrication  
309 tolerances, a gap of 2 mm between the tube and the shear-key was specified in the FE  
310 models, as reported in shear-keyed IMC [28,29] and post-tensioned frames [51,82]  
311 studies.

## 312 **4.3 Tubes geometry**

313 The geometrical details of the shear-keyed tube are depicted in **Fig. 7**. Since the purpose  
314 of the study was to determine the efficacy of shear keys, various parameters are  
315 designed according to **Table 4**. The standard  $L_c$  for shear-keyed tubes was determined  
316 to be 1.5 m, varying from 1.5 to 1.0, 1.2, 1.8, 2.4, 3.0, and 3.6 m. The case studies in  
317 **Fig. 1(a)** utilized tubular columns with a lower  $D/t_c$  and  $L_c/r_c$  ratio to improve their

318 slenderness and stability, avoid flexural buckling and ensure a 50-year design life of  
 319 MSS against 8-degree seismic forces. Therefore,  $D$ ,  $B$ , and  $t_c$  of the tube's cross-section  
 320 varied from  $200 \times 200 \times 8$  to  $200 \times 200 \times 5$ ,  $200 \times 200 \times 7$ ,  $200 \times 200 \times 9$ ,  $200 \times 200 \times 10$ ,  
 321  $150 \times 150 \times 10$ ,  $180 \times 180 \times 10$ ,  $220 \times 220 \times 10$ ,  $250 \times 250 \times 10$ ,  $160 \times 80 \times 8$ ,  $200 \times 120 \times 8$ ,  
 322  $220 \times 140 \times 8$ , and  $250 \times 180 \times 8$  mm. In comparison, the size of the connecting plate  
 323 remained constant, measuring  $524 \times 484 \times 20$  mm.



324 **Fig. 7** Developed FEM of shear-keyed tubes

325 **4.4 Tubes developed FEM**

326 The FEM depicted in **Fig. 7** consists of shear keys welded to connecting plates, steel  
 327 tubes, and connecting plates. Since the hot-rolled section is used in the prototype project,  
 328 all components meshed with C3D8R elements following the Refs. [28,29] on shear-  
 329 keyed frames and Refs. [58] and [12,13] on tubular walls. All corners around the tube  
 330 or shear key cross-section thickness were partitioned to form the structured mesh.  
 331 Corners have smaller element sizes than other regions, suggesting a minimum mesh  
 332 size of  $30 \times t \times t$  ( $\text{mm}^3$ ). The uniform mesh was applied to other regions; therefore, they  
 333 had bigger element sizes than corners, providing them a maximum mesh size of  
 334  $30 \times 30 \times t$  ( $\text{mm}^3$ ).  
 335

336 Upper and lower connecting plates are always flat, so their movement in each direction  
337 was constrained. To permit vertical displacement, the bottom section was allowed to  
338 move vertically. Surface-based kinematic coupling constraints were attained by  
339 defining the reference nodes on the centers of the lower and upper connecting plates  
340 and restraining all degrees of freedom at the coupling nodes. Connecting plates and  
341 shear keys established surface-to-surface contact with ties to fuse them and constrain  
342 their relative motion. The column's interaction with the connecting plates and shear  
343 keys was represented as surface-to-surface (standard), using "hard contact" as the  
344 normal behavior and "penalty friction formulation" as tangential with a friction  
345 coefficient of 0.3. On the other hand, the "no key" model assumed a tube welded to the  
346 plates, achieved by the surface-to-surface tie constraint. Q345 was employed in the  
347 shear-keyed tube design of the authors' prototype project since it is often used in the  
348 Chinese industry. Similarly, according to ASTM, Q345 is substituted for S355, as  
349 their strength, stiffness, and ductility are nearly identical [83]. Consequently, the yield  
350 and ultimate strengths of 380 and 503 MPa for the shear-keyed tubes were obtained by  
351 averaging the values of specimens made of S355, i.e., 140×80×4, 140×80×6, 160×80×5,  
352 200×80×10 listed in **Table 2** from AS19-AS22 as reported in Refs. [12–14,58]. The  
353 modulus of elasticity was determined to be 206 GPa. These values were used to  
354 maintain consistency with the MSS shear-keyed building design.

355 When imperfection is related to the first buckling mode, the bifurcation point closely  
356 resembles the first eigenvalue estimated for the ideal structure [84]. According to Ref.  
357 [62], the first eigenmode is more significant and is considered the most crucial in elastic  
358 buckling, so it is introduced and scaled as the structure's initial defect. Another study  
359 on IMC's axial compression behavior in MSS used the first mode to input imperfection  
360 amplitude [10]. According to validated test sources in Refs. [56,57], tests on MSB's

361 IMC in Ref. [10], and numerical studies in Ref. [84] and [62], imperfection application  
362 in the first buckling mode is a reliable, critical, and extensively employed approach.  
363 This study used the lowest buckling mode for initial geometric imperfections to acquire  
364 reliable outcomes. The initial geometric imperfection of tubular walls was obtained  
365  $L_c/600$  by comparing the load-shortening curves of FE to those of tests reported by Hou  
366 et al. [58] and Khan et al. [12,13]. Thus, shear-keyed tubes that were built as hot-rolled  
367 sections used a magnitude of  $L_c/600$  to perform the parametric study.

#### 368 **4.5 Typical load-shortening behavior**

369 Generalized load-shortening curves are depicted in **Fig. 8**, illustrating the existence of  
370 linear elastic (I), nonlinear (II), and recession (III) zones for type A and B curves. The  
371 recession is a state of the load-shortening curves after the ultimate/peak stage with a  
372 subsequent trough characterized by a significant drop in the tubes' load-carrying  
373 capacity that can persist to larger end-shortening values. This is specified as post-  
374 ultimate or post-peak dropping or falling branches, consistent in Refs. [85–91]. The  
375 figure indicates that load increases linearly during the initial linear state with shortening  
376 till yield stage  $P_y$ . It implies that type A FEMs had a shorter elastic branch and yielded  
377 sooner than type B. This shortening could be caused by the decreased compression  
378 strength of shear-keyed tubes, reducing yield and ultimate strengths. The stiffness  
379 reduction of curves started at  $P_y$  because stresses on the several locations on tubes  
380 exceeded the material yield strength. Following  $P_y$  until  $P_u$ , the curves have a parabolic  
381 shape; at the same time, local buckling becomes apparent as the tube reaches  
382 compression capacity. Shear-keyed columns undergo local plastic buckling after stage  
383 II. In contrast to stage I, stage II of type A curve FEM is more prolonged than type B,  
384 illustrating the superior ductility of type A FEMs. This is evident from **Table 4**. This is  
385 because increasing the rigidity or decreasing the slenderness with thicker or shorter

386 tubes or longer and thicker shear-key improves compressive strength but impairs  
387 ductility. During stage II, the tube attains  $P_u$  and undergoes local inward or outward  
388 buckling. Stage III is characterized by a decrease in the load that the tube can support  
389 (load-carrying capacity) and significant local buckling. Similarly, at the post-ultimate  
390 stage, the  $DI$  can be compared. The capacity of type B FEMs is noticeably lower than  
391 that of type A, indicating that tubes cannot offer resistance after buckling has been  
392 initiated.

393 Shear-keyed tubes have varying flexural stiffness on ends and mid that generate non-  
394 homogeneity and non-uniform stress distribution [92]. This reduces end rotational  
395 stiffness, increases slenderness, and weakens shear-keyed tubes relative to tubes  
396 without shear keys [80]. Besides, semi-rigid shear keys with low tube-end stiffnesses  
397 generate stresses in columns subjected to axial compression, resulting in yield and  
398 ultimate capacity reductions [35]. This weakening effect on tubes is consistent with  
399 Refs. [12–14,58]. Shear stresses in columns are increased in tubes with non-welded  
400 shear keys compared to tubes without shear keys, and compressive behavior is degraded.  
401 The shear keys transmit shear forces till considerable tube deformation, with force  
402 increasing as the tube deforms [93]. Neglecting shear stresses or assuming welding of  
403 shear-keyed IMC to tubes would overestimate buckling strength [94].

404

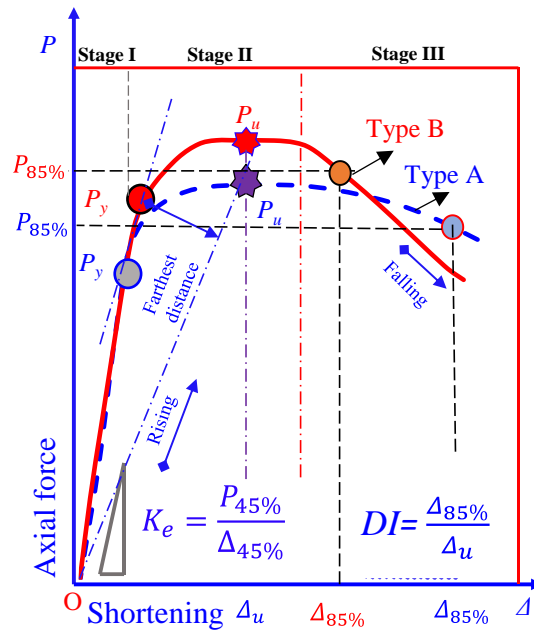


Fig. 8 Typical compressive behavior of shear-keyed tubes

#### 4.6 Typical failure modes

Supplementary Fig. B1 organizes the failure modes of all 109 FEMs from No key to

FS-108. Moreover, Fig. 9(a-f) summarizes graphs that gather similar column behavior

per parametric studies in Table 4. Comparing tubes with and without shear keys reveals

that tubes without shear-keyed IMC failed with IB or OB, whereas shear-keyed tubes

faced sinusoidal IB and OB, the same on opposite and opposite on adjacent faces. This

failure was more visible in short columns than in long tubes. Long or rectangular tubes

with substantially higher cross-section lengths than widths display stress localization

near the loading end; thus, failure starts on shear-key edges in the longer direction and

spreads to the shorter side. This is because the longer side has a lower flexural stiffness.

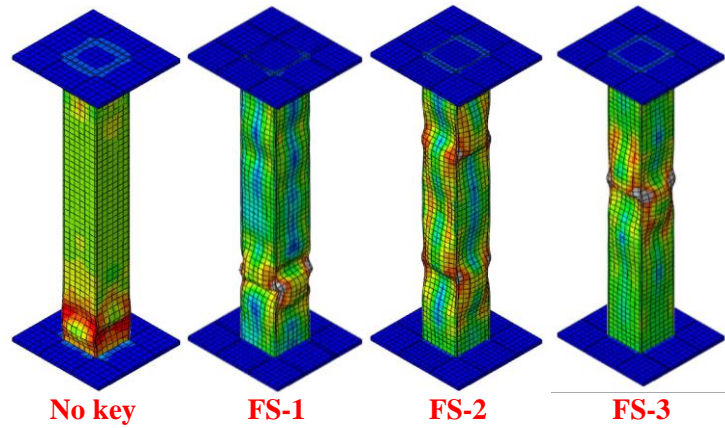
If the buckling resistance of tubes is considerably raised by increasing the shear-key

height and thickness and total stiffness of the column, the failure mode extends away

from the edges, and the behavior becomes uniform. Additionally, the influence of

varying imperfection values on failure behavior was not evident; however, load-

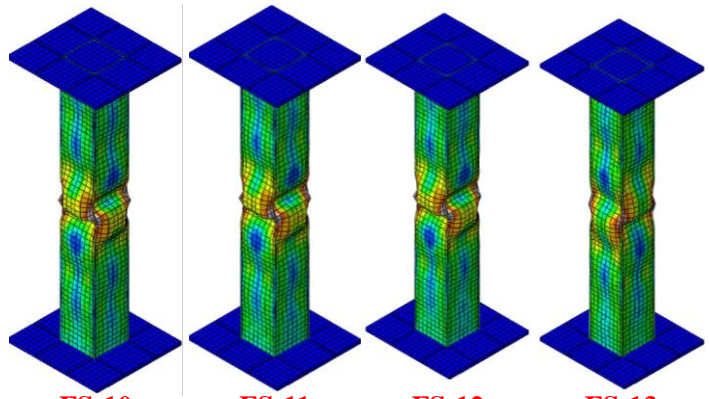
shortening curves seem extremely sensitive.



**No key**      **FS-1**      **FS-2**      **FS-3**

**(a) Effect of shear-key thickness ( $t_f$ )**

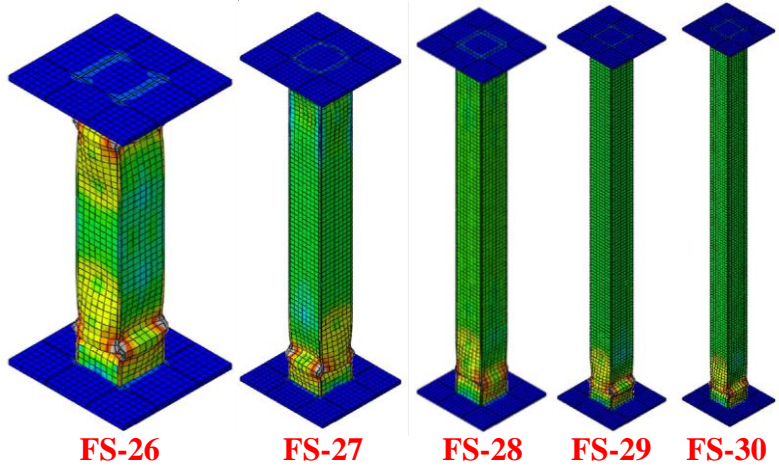
422



**FS-10**      **FS-11**      **FS-12**      **FS-13**

**(b) Effect of shear-key height ( $L_f$ )**

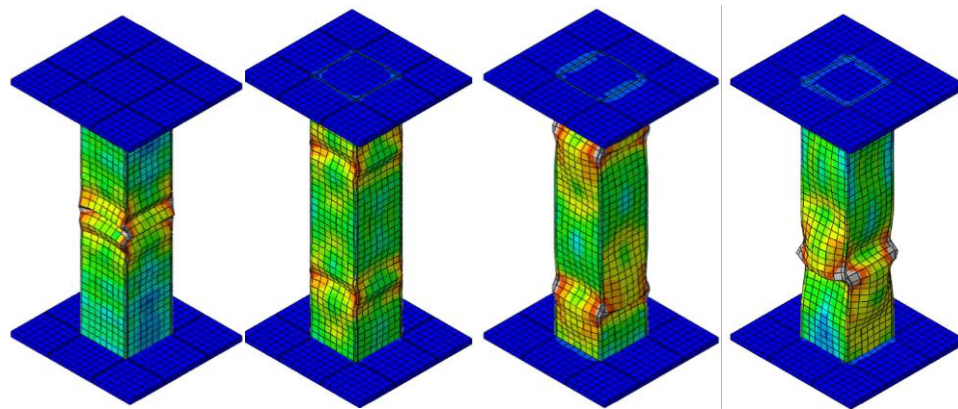
423



**FS-26**      **FS-27**      **FS-28**      **FS-29**      **FS-30**

**(c) Effect of tube height ( $L_c$ )**

424



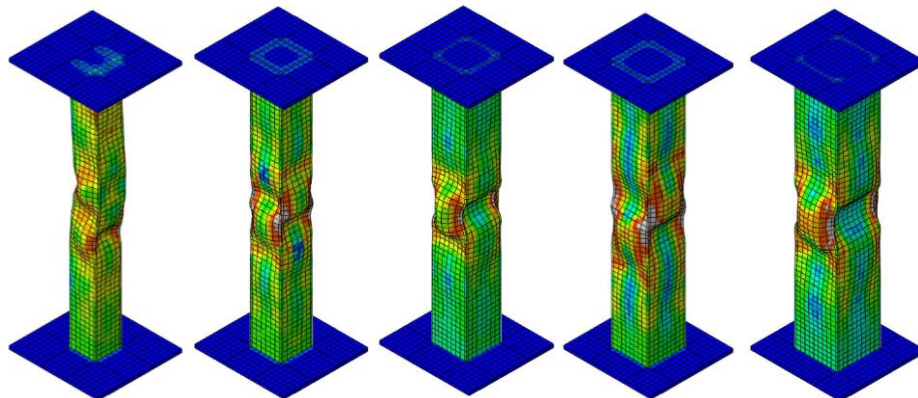
FS-58

FS-59

FS-60

FS-61

(d) Effect of tube thickness ( $t_c$ )



FS-70

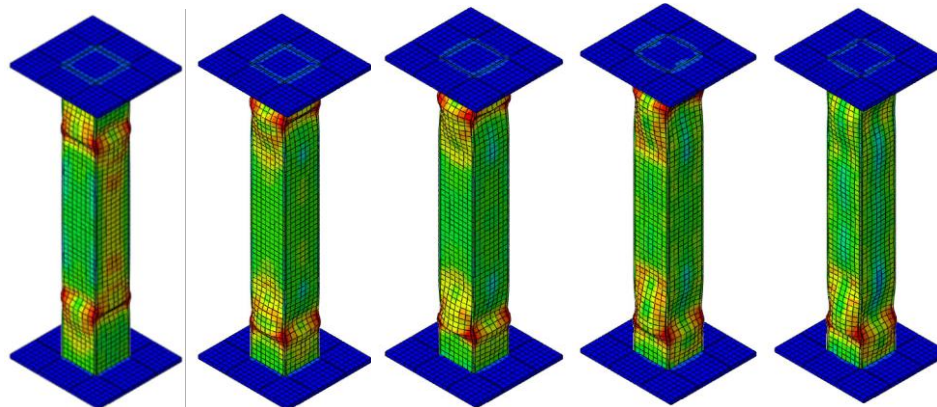
FS-71

FS-72

FS-73

FS-74

(e) Effect of tube  $D \times B$



FS-97

FS-98

FS-99

FS-100

FS-101

(f) Effect of imperfection

425

426

427

Fig. 9 Shear-keyed tubes' typical failure modes

## 428 4.7 Discussions using parametric analysis

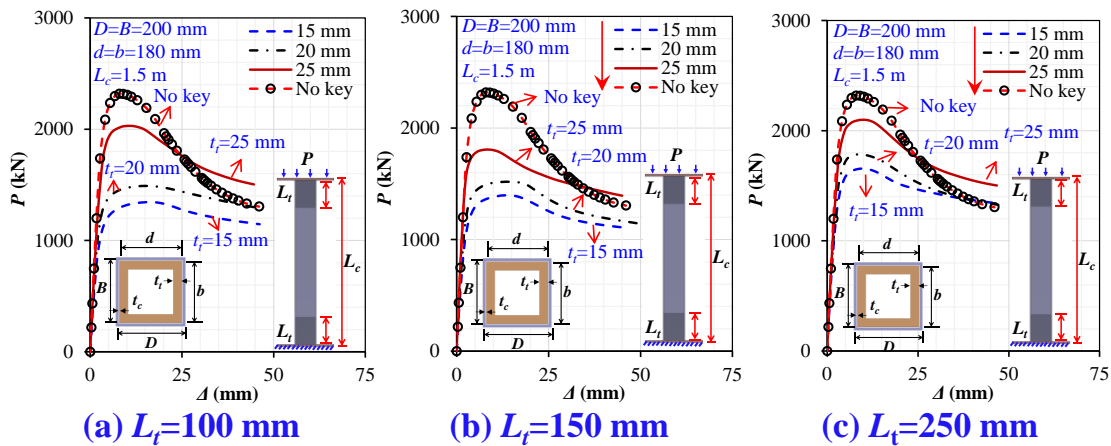
### 429 4.7.1 Shear-key thickness effects ( $t_t$ )

430 **Figure 10(a-c)** illustrates the influence of the  $t_t$  (i.e., 15, 20, and 25 mm) on the  $P-\Delta$

431 curves. The effect on the  $P_u$ ,  $K_e$ ,  $\Delta_u$ , and  $DI$  ratios with varied  $L_t$  (i.e., 100, 150, and 250

432 mm) is shown in **Fig. 11(a-d)**. Raising  $t_t$  has beneficial effects on  $P_u$  and  $K_e$  but shows

433 a weaker relationship and has a significant variation on  $\Delta_u$ . As the  $t_t$  rises from 15 to 20  
 434 and 25 mm, the  $P_u (K_e)$  improves by 11% to 51% (14% to 32%) with 100 mm  $L_t$ .  
 435 Increasing the  $t_t$  reduces slenderness and raises compressive resistance. Furthermore,  
 436 altering  $t_t$  had a varying effect on  $DI$  ratios due to obvious scatters except with 250 mm  
 437  $L_t$ . Moreover, the impact on  $\Delta_u$  showed an inconsistent relationship, such as unfavorable,  
 438 with falls for 100 mm and favorable with rise for 150 mm  $L_t$ . Because increased shear-  
 439 keyed IMC stiffness causes plastic buckling/yielding. This improves tube yield strength  
 440 while reducing buckling strain, hence impairing  $\Delta_u$ . Comparing tubes with and without  
 441 shear keys in **Fig. 10** and **Table 4** reveals that shear-keyed tubes reduce  $P_u$  and  $K_e$ . It is  
 442 because the presence of non-welded shear-keyed IMC affects rotational stiffness and  
 443 slenderness and produces stresses in columns, resulting in yield and ultimate capacity  
 444 reductions, as Refs. [35], [92], [80], [93], and [94].



446 **Fig. 10** Effect of  $t_t$  on  $P$ - $\Delta$  curves for given  $L_t$

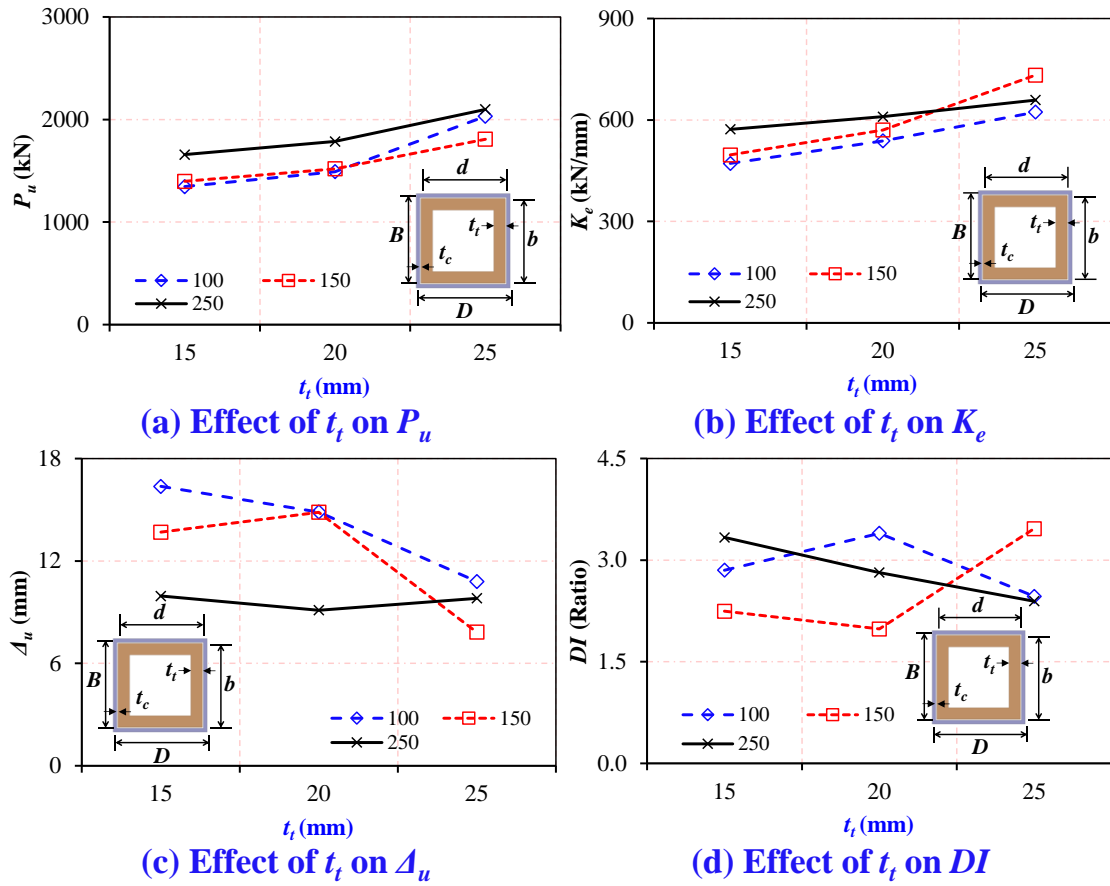


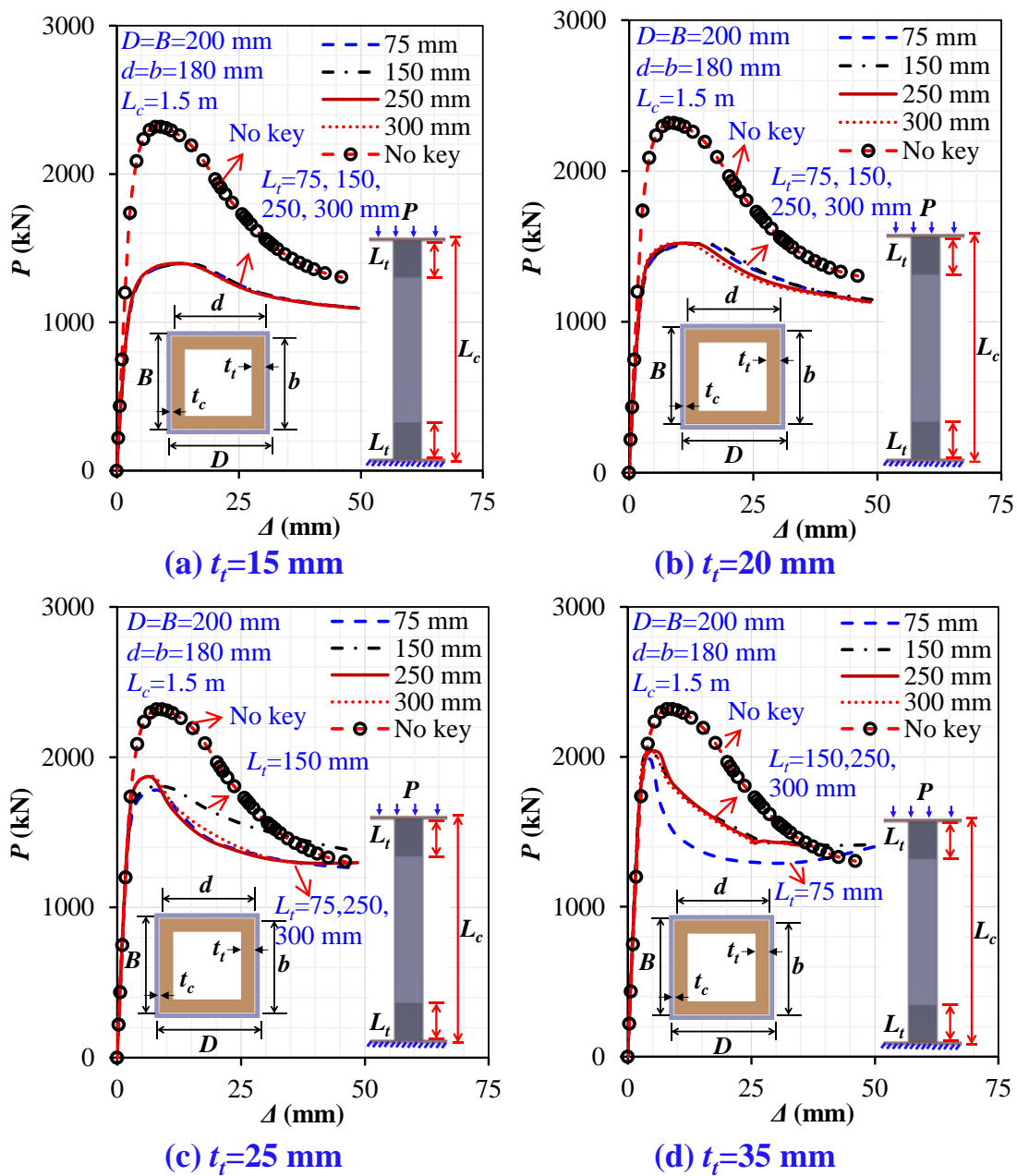
**Fig. 11** Effect of  $t_t$  on  $P_u$ ,  $K_e$ ,  $\Delta_u$ , and  $DI$

447  
448

449 4.7.2 Shear-key height effects ( $L_t$ )

450 **Figure 12(a-d)** demonstrates the  $L_t$  (i.e., 75, 150, 250, and 300 mm) impact on  $P$ - $\Delta$   
 451 curves. **Figure 15(a-d)** illustrates a variation in  $P_u$ ,  $K_e$ ,  $\Delta_u$ , and  $DI$  ratios with various  $t_t$   
 452 (15, 20, 25, and 35 mm). Raising  $L_t$  has a minor effect on  $P_u$  ( $K_e$ ) upto 5% (2%) but a  
 453 noticeable detrimental effect on  $\Delta_u$ . This impact is more apparent when a larger value  
 454 of  $t_t$  is used. Increasing the  $L_t$  improves compressive resistance due to the enlargement  
 455 of shear keys, making a tube-connecting plate joint stiffer. Furthermore, modifying  $L_t$   
 456 possessed a weaker relationship with the  $DI$ , yet, the impact with thicker keys was  
 457 noteworthy because longer and thicker shear keys extend the recession stage. The rise  
 458 of  $L_t$  is weakly related to  $\Delta_u$ . Increasing shear-key length improves tube yield strength  
 459 while reducing buckling strain, which influences ductility. **Figure 12** and **Table 4** show  
 460 that the shear keys significantly reduce tubes  $P_u$  ( $K_e$ ) up to 42% (30%) for  $t_t$  of 15 mm

461 compared to tubes without shear keys; nevertheless, the drop in percentage rise is  
 462 evident with larger shear keys due to their improved compressive behavior.



464 **Fig. 12** Influence of  $L_t$  on  $P$ - $\Delta$  curves for given  $t_t$   
 465

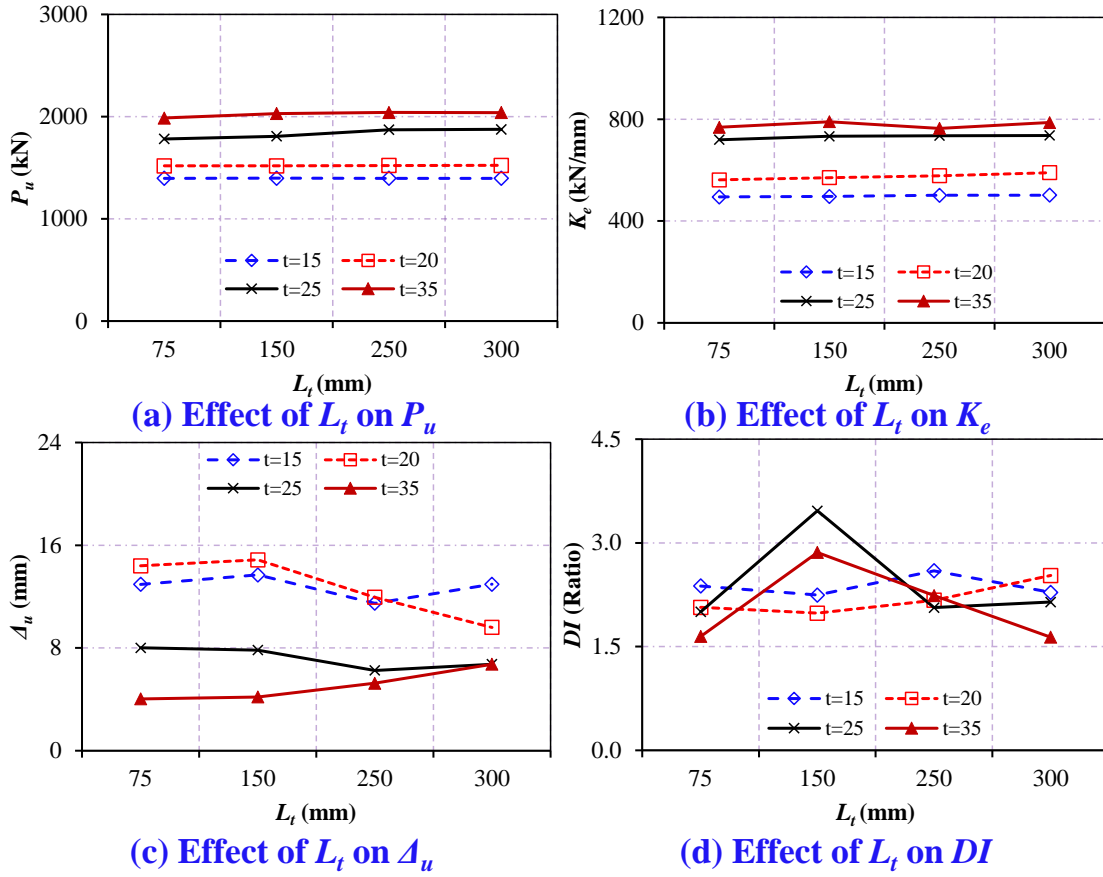
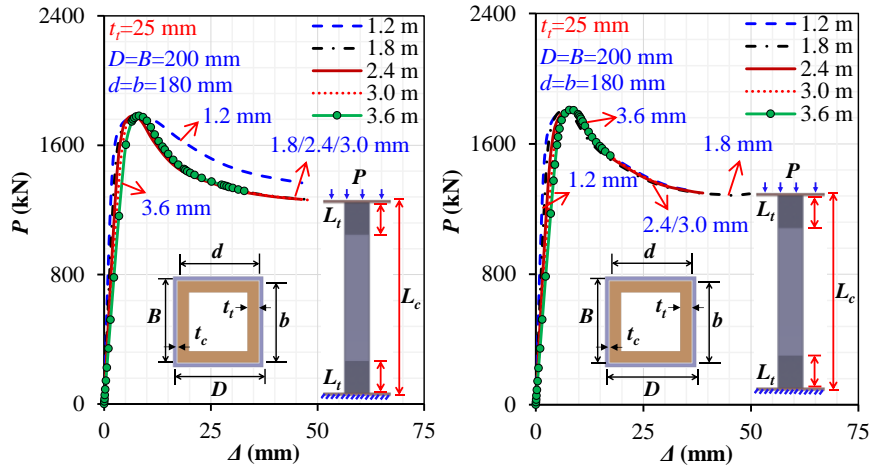


Fig. 13 Influence of  $L_t$  on  $P_u$ ,  $K_e$ ,  $\Delta_u$ , and  $DI$

466  
467

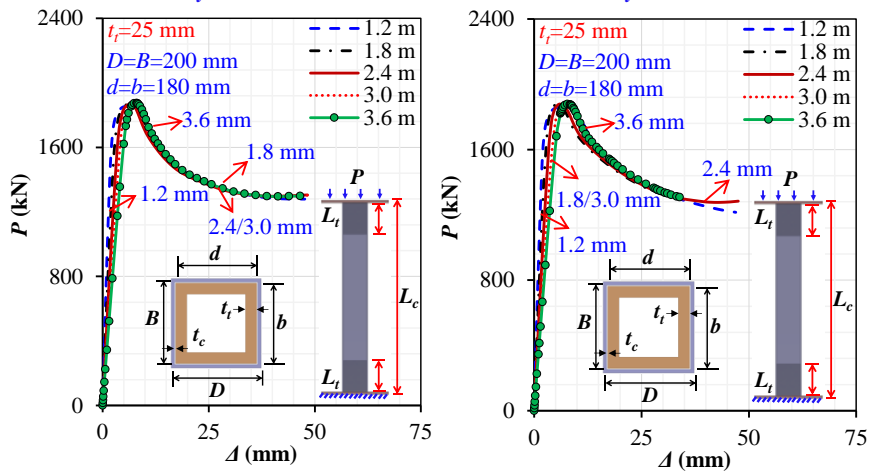
#### 4.7.3 Column's height ( $L_c$ )

469 **Figure 14(a-d)** displays the effect of  $L_c$  (i.e., 1.2, 1.8, 2.4, 3.0, and 3.6 m) on the  $P$ - $\Delta$   
 470 graphs. **Figure 15(a-d)** summarizes the variation trend of  $P_u$ ,  $K_e$ ,  $\Delta_u$ , and  $DI$  ratios with  
 471 varying  $L_t$  (i.e., 75, 150, 250, and 300 mm). Growing  $L_c$  showed no noticeable influence  
 472 on  $P_u$  while linearly reducing  $K_e$  and  $DI$ . Raising  $L_c$  decreased  $K_e$  upto 61% by  
 473 increasing the  $L_c/r$  ratio, making the column more susceptible to the shear-keyed IMC's  
 474 shear effect. Besides, tube-key boundary interactions also become weaker.



(a)  $L_t=75$  mm

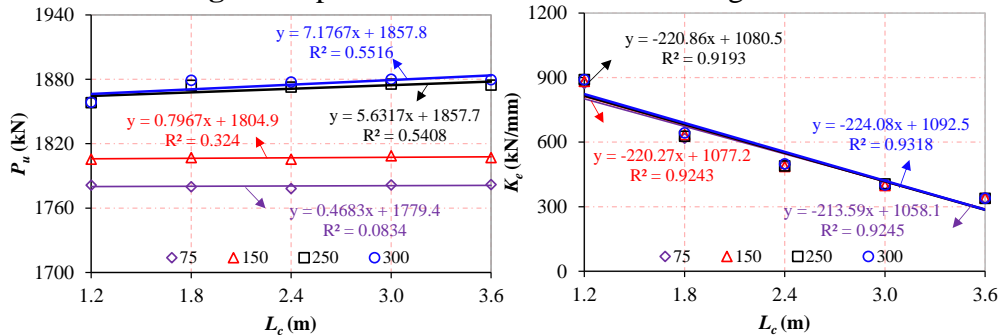
(b)  $L_t=150$  mm



(c)  $L_t=250$  mm

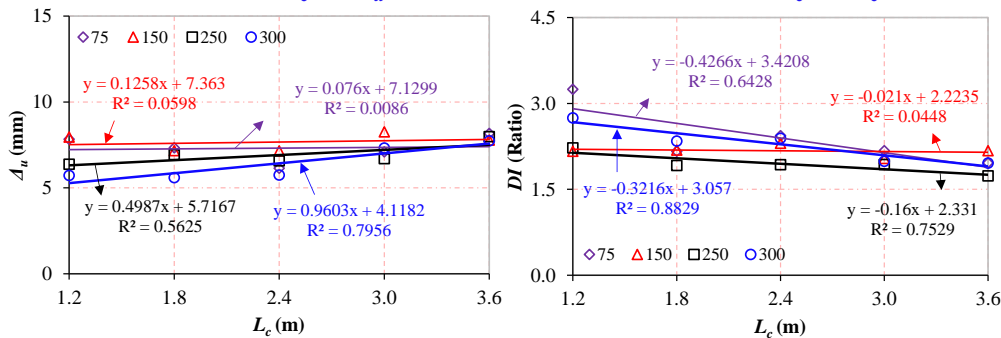
(d)  $L_t=300$  mm

**Fig. 14** Impact of the  $L_c$  on  $P-\Delta$  curves for given  $L_t$



(a) Effect of  $L_c$  on  $P_u$

(b) Effect of  $L_c$  on  $K_e$



(c) Effect of  $L_c$  on  $\Delta_u$

(d) Effect of  $L_c$  on  $DI$

**Fig. 15** Impact of the  $L_c$  on  $P_u$ ,  $K_e$ ,  $\Delta_u$ , and  $DI$

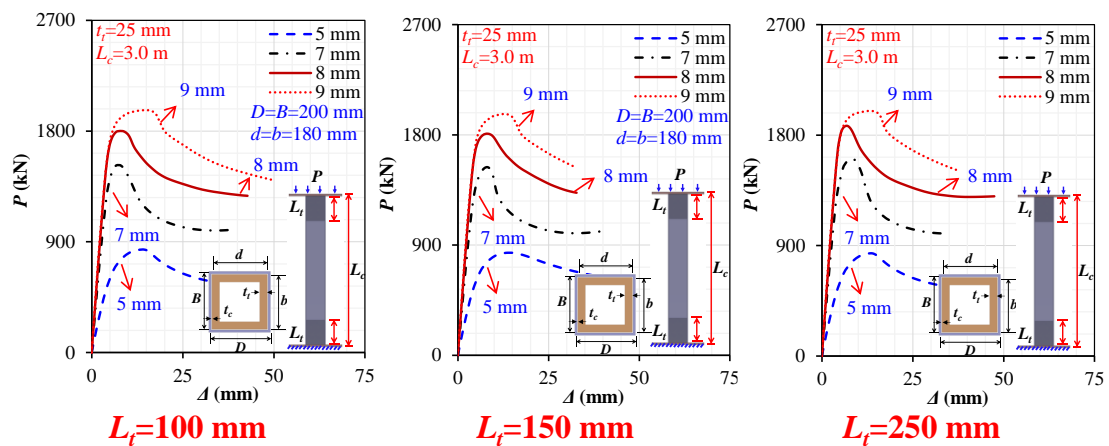
475

476  
477

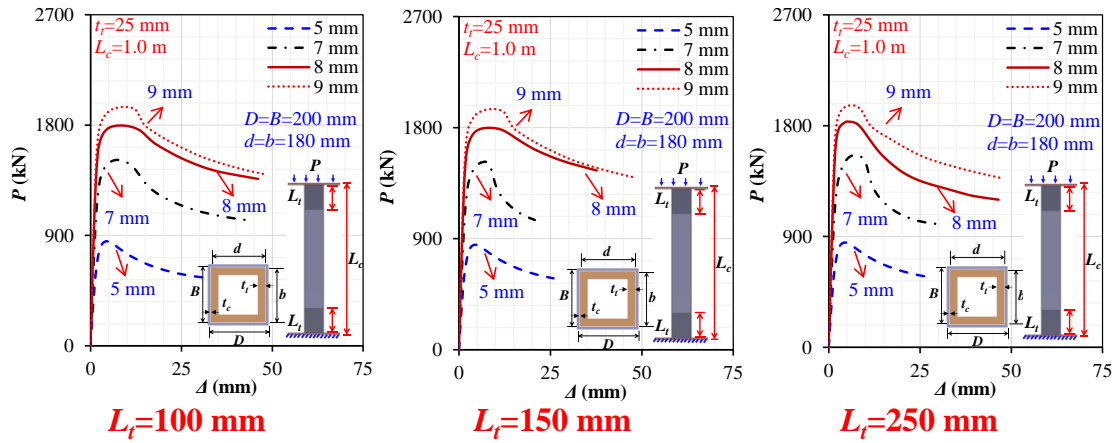
478  
479

480 4.7.4 Column's thickness ( $t_c$ )

481 The effects of varying  $t_c$  (i.e., 5, 7, 8, and 9 mm) for given  $L_c$  (i.e., 1 and 3 m) and  $L_t$   
 482 (i.e., 100, 150, and 250 mm) on the  $P-\Delta$  graphs are depicted in **Fig. 16(a,b)**. **Figure**  
 483 **16(c,d)** plots the varying trends of  $P_u$ ,  $K_e$ ,  $\Delta_u$ , and  $DI$  ratios. It demonstrates a linear rise  
 484 in  $P_u$  and  $K_e$  as the  $t_c$  improves. For the 3 m  $L_c$ , the  $P_u$  ( $K_e$ ) increased upto 135% (207%)  
 485 and 129% (147%) for the  $L_c$  of 1 m. Simultaneously,  $DI$  shows a weaker relationship;  
 486 while  $\Delta_u$  is fallen for 3 m  $L_c$  columns. However,  $DI$  shows a larger scatter, and  $\Delta_u$  has  
 487 risen for 1 m  $L_c$  columns. Increasing  $t_c$  decreases cross-sectional slenderness ( $D/t_c$ ), or  
 488  $L_c/r$ , which improves buckling resistances of columns, thereby enhancing the tubes'  
 489 strength and stiffness. Compared to short tubes, tubes with a larger  $L_c$  exhibit a decrease  
 490 in ductility due to higher member slenderness, which makes the column more  
 491 susceptible to non-uniform stress distribution, localization, and non-yielding due to the  
 492 shear keys' apparent shear effect. Moreover,  $D/t_c$  falls from 40 to 22, as  $t_c$  rises from 5  
 493 to 9 mm, changing the cross-section from Class 4 to 1.

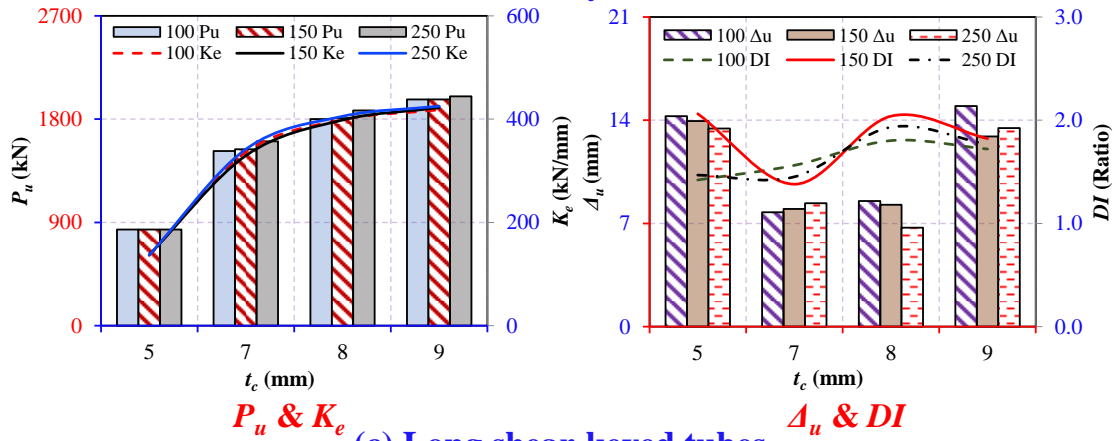


494



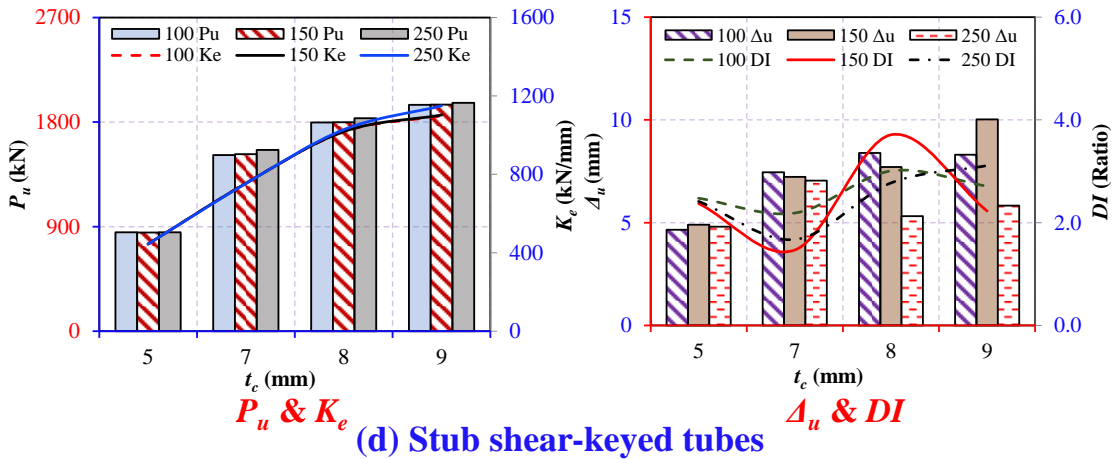
(b) Stub shear-keyed tubular columns

495



(c) Long shear-keyed tubes

496



(d) Stub shear-keyed tubes

497

498

Fig. 16 Effect of  $t_c$  on  $P-\Delta$ ,  $P_u$ ,  $K_e$ ,  $\Delta_u$ , and  $DI$  relationships

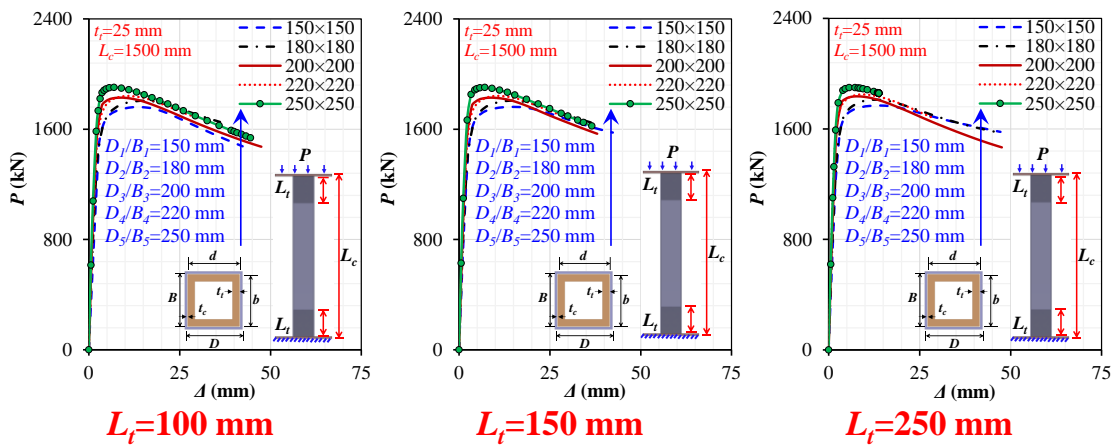
499

4.7.5 Tube cross-section ( $D \times B$ )

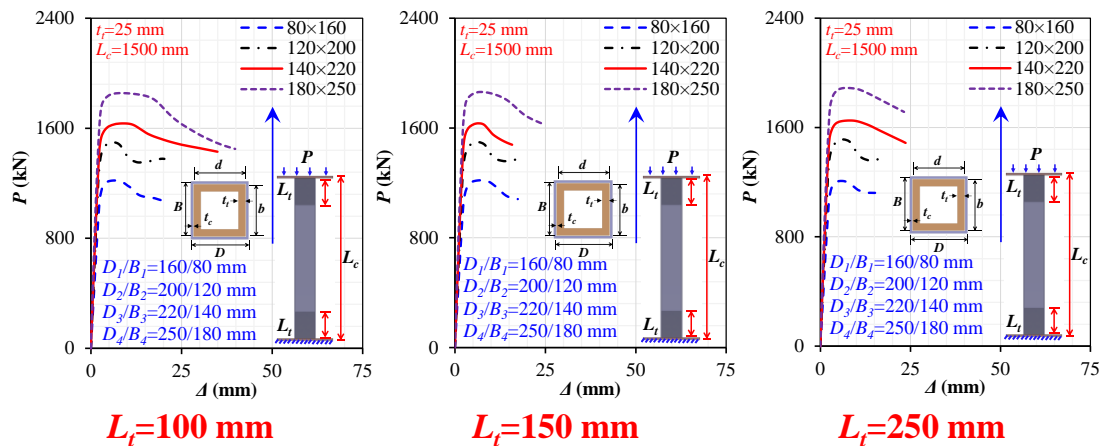
500

Figure 17(a-d) depicts the outcome of modifying  $D$  and  $B$  with different  $L_t$  of 100, 150, 501 and 250 mm. It demonstrates that as the  $D$  and  $B$  increase from 150 to 180, 200, 220, 502 and 250 mm,  $P_u$  ( $K_e$ ) increases linearly upto 8% (78%). Similarly, a 52% (70%) rise is 503 noticed with enhancing  $B/D$  to 80/60, 120/200, 140/220, and 180/250 mm. This is so

504 that buckling resistances can be improved by raising  $D$  and  $B$ , which also decreases  
 505 slenderness. Simultaneously, square tubes  $\Delta_u$  showed a decrement of upto 56%,  
 506 whereas  $DI$  increased by upto 140%. It is because a larger cross-section undergoes  
 507 yielding, decreasing buckling strain but prolonging recession behavior. On the contrary,  
 508 rectangular tubes  $\Delta_u$  and  $DI$  showed a weaker relationship with an increase or decrease  
 509 in  $D$  or  $B$ . This might be due to varying non-uniform stress localization on shear keys  
 510 on the longer side that could lead to premature buckling. Also,  $D/t_c$  increases from 15  
 511 to 18, 20, and 25 when  $D/B$  is increased from 150/150 to 180/180, 200/180, 220/220,  
 512 and 250/250 mm with a  $t_c$  of 10 mm. The cross-section class changes when  $D/B$   
 513 increases from 160/80 to 200/120, 220/140, and 250/180 with 8 mm  $t_c$ , raising  $D/t_c$   
 514 increases from 20 to 25, 27, and 31.



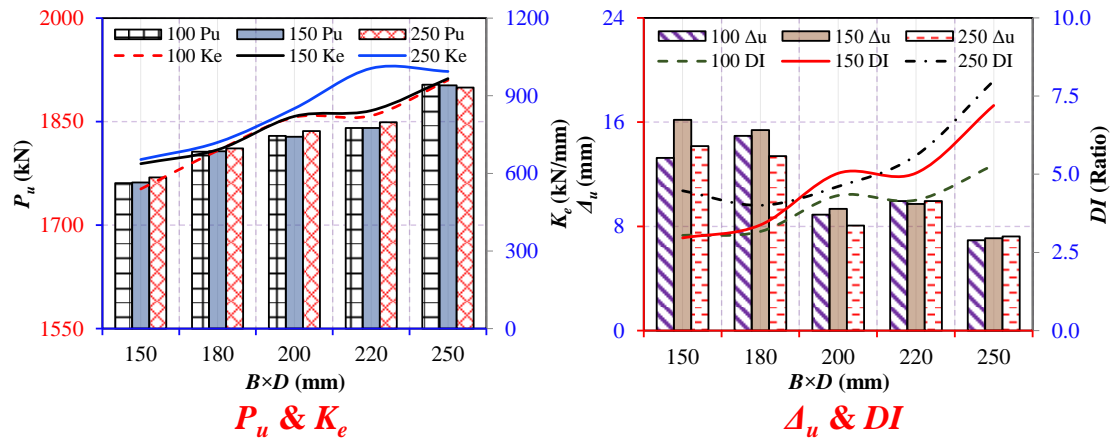
(a) Square shear-keyed tubes



(b) Rectangular shear-keyed tubes

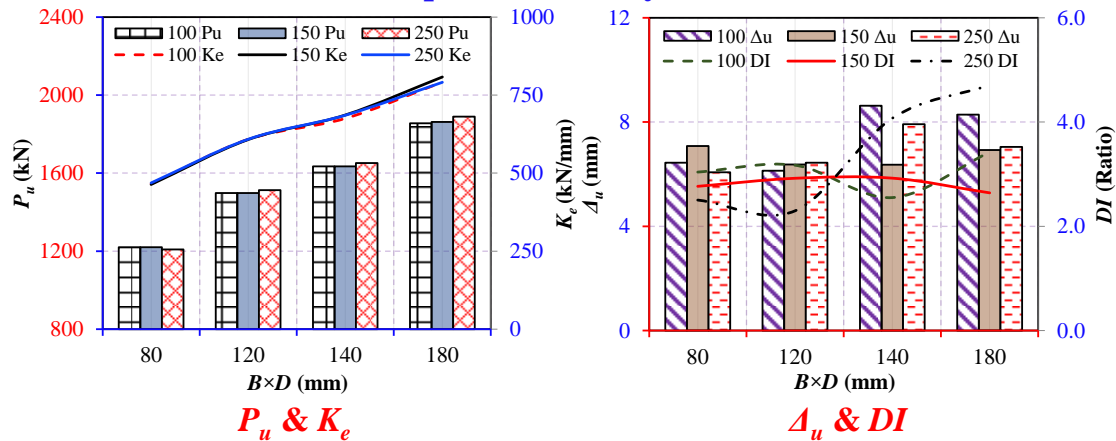
515

516



(c) Square shear-keyed tubes

517



(d) Rectangular shear-keyed tubes

518

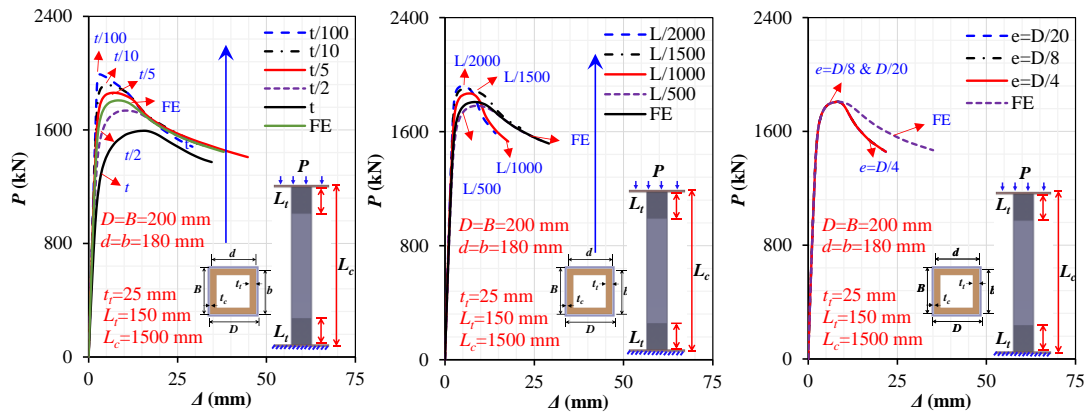
519

Fig. 17 Influence of  $D \times B$  on  $P-\Delta$ ,  $P_u$ ,  $K_e$ ,  $\Delta_u$ , and  $DI$  relationships

520 4.7.6 Initial imperfection

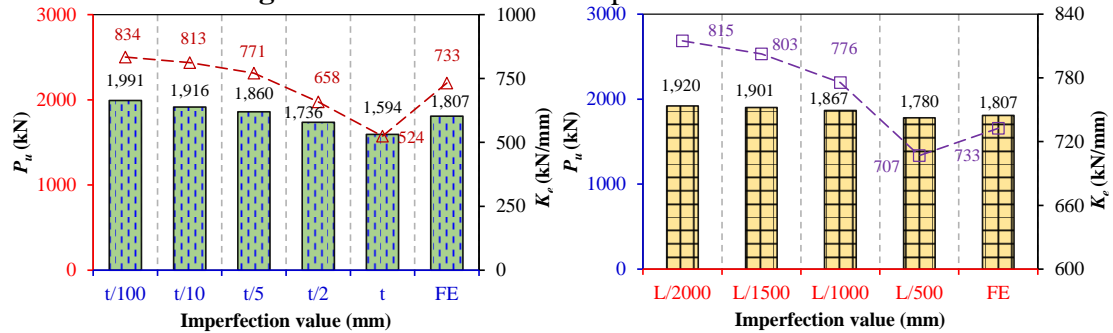
521 Compared to TSS, initial geometric imperfection on the shear-keyed tubes influences  
 522 manufacturing, installing, and assembling MSS due to offsite fabrication and onsite  
 523 installation flaws, impacting performance [10]. Given that the shear-keyed module  
 524 column primarily transfers the structural loads to IMC, the initial imperfections issue is  
 525 crucial for corner-supported MSS and has significant concerns [95]. Consequently, the  
 526 parametric study explores shear-keyed tube compression behaviors for excessive initial  
 527 imperfections as per Ref. [10]. Theofanous and Gardner [57] proposed that member  
 528 thickness ( $t_c$ ) or height ( $L_c$ ) and applied eccentricity ( $e$ ) contribute to local and global  
 529 imperfections. This research chose imperfection values as tube thickness ( $t_c$ ) of  $t_c/100$ ,  
 530  $t_c/10$ ,  $t_c/5$ ,  $t_c/2$ , and  $t_c$ ; tube height ( $L_c$ ) of  $L_c/2000$ ,  $L_c/15000$ ,  $L_c/1000$ , and  $L_c/500$ ; and

531 eccentricity ( $e$ ) of  $D/20$ ,  $D/8$ , and  $D/4$ , and compared with the validated FE outcomes  
532 that used an initial magnitude of  $L_c/600$ . **Figure 18(a-c)** summarizes the influences on  
533  $P$ - $\Delta$  graphs, whereas **Fig. 19(a-f)** shows variation in  $P_u$ ,  $K_e$ ,  $\Delta_u$ , and  $DI$  trends. Increasing  
534 value from  $t_c/100$  to  $t_c/10$ ,  $t_c/5$ ,  $t_c/2$ , and  $t_c$  lowered  $P_u$  ( $K_e$ ) by upto 20% (37%).  
535 Compared to  $L_c/600$ ,  $t_c/100$ ,  $t_c/10$ , and  $t_c/5$  overestimated  $P_u$  ( $K_e$ ) by upto 10% (14%),  
536 while  $t_c/2$  and  $t_c$  underestimated by upto 12% (28%). Whereas increasing from  $L_c/2000$   
537 to  $L_c/1500$ ,  $L_c/1000$ , and  $L_c/500$  dropped  $P_u$  ( $K_e$ ) by upto 7% (13%). Moreover,  $L_c/2000$   
538 to  $L_c/1500$  and  $L_c/1000$  overestimated  $P_u$  ( $K_e$ ) by upto 6% (11%), while  $L_c/500$  was  
539 underestimated by 1% (3%) compared to  $L_c/600$ . Additionally, increasing from  $t_c/100$   
540 to  $t_c/10$ ,  $t_c/5$ ,  $t_c/2$ , and  $t_c$  raised  $\Delta_u$  by upto 385% but decreased  $DI$  upto 57%. While  
541 rising from  $L_c/2000$  to  $L_c/1500$ ,  $L_c/1000$ , and  $L_c/500$  lowered  $\Delta_u$  ( $DI$ ) upto 69% (26%).  
542 Compared to  $L_c/600$ ,  $t_c/100$  and  $t_c/10$  overestimated  $\Delta_u$  and underestimated  $DI$ , while  
543  $t_c/2$  and  $t_c$  underestimated  $\Delta_u$  and overestimated  $DI$ . Likewise,  $L_c/2000$ ,  $L_c/1500$ , and  
544  $L_c/1000$  overestimated  $\Delta_u$  and  $DI$ , but  $L_c/500$  underestimated  $\Delta_u$ . This is because  
545 geometric imperfection accounts for secondary structural behavior, leading to  
546 significant strength and stiffness degradation [57,96]. Furthermore, the rising  $e$  from  
547  $D/20$  to  $D/8$  and  $D/4$  showed a non-apparent influence due to flat platens. Compared to  
548 the FE findings on shear-keyed tubes, the initial imperfection of  $L_c/500$  is the closest  
549 indicator of actual compression behavior obtained by  $L_c/600$  in the referenced study.  
550 Simultaneously,  $t_c/5$  and  $L_c/1000$  overestimated, while  $t_c/2$  and  $L_c/500$  underestimated  
551 it.



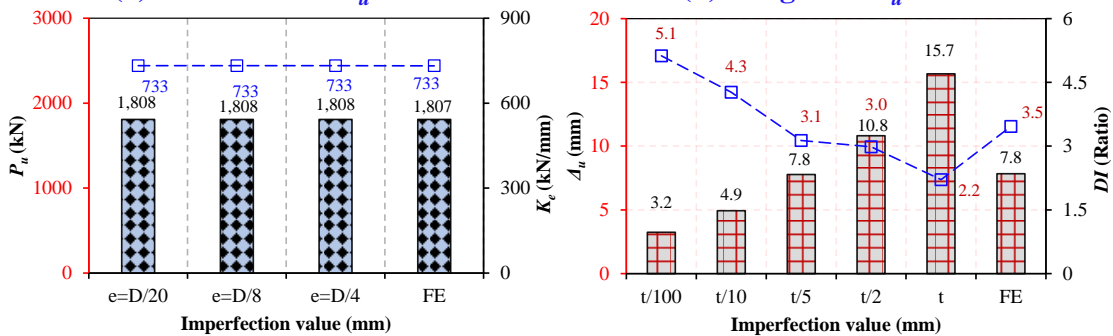
(a) Local imperfection  $t_c$  (b) Local imperfection  $L_c$  (c) Geometric imperfection  $e$

**Fig. 18** Influence of initial imperfection  $P-\Delta$  curves



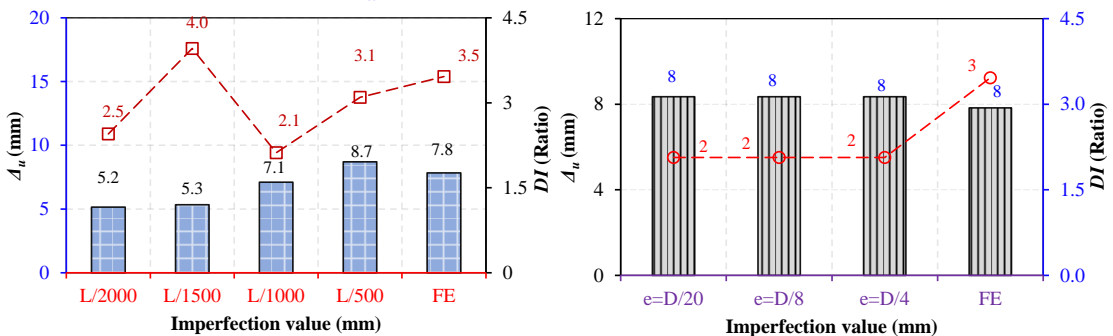
(a) Thickness on  $P_u$  &  $K_e$

(b) Length on  $P_u$  &  $K_e$



(c) Eccentricity on  $P_u$  &  $K_e$

(d) Thickness on  $\Delta_u$  &  $DI$



(e) Length on  $\Delta_u$  &  $DI$

(f) Eccentricity on  $\Delta_u$  &  $DI$

**Fig. 19** Influence of initial imperfection on  $P_u$ ,  $K_e$ ,  $\Delta_u$ , and  $DI$  relationships

554 **5 Analytical research on ultimate resistance predictions using design standards**

555 The approach presented in **Fig. 20** has been widely utilized in Ref. [97], [57], and [98]

556 to evaluate the applicability of design standard prediction equations. In EC3 [99],

559 members' cross-sectional ( $P_{u,c}$ ) and buckling ( $P_{u,b}$ ) resistance via Eqns. 5~7,  
 560 representing EC3-C and EC3-B, are used to design shear-keyed tubes:

$$P_{u,c} = f_y A_s (\text{or } A_{eff}) / \gamma_M ; P_{u,b} = \chi f_y A_s (\text{or } A_{eff}) / \gamma_M \quad (5)$$

$$\chi = 1 / [\phi + (\phi^2 - \bar{\lambda}^2)^{0.5}] \leq 1 \quad (6)$$

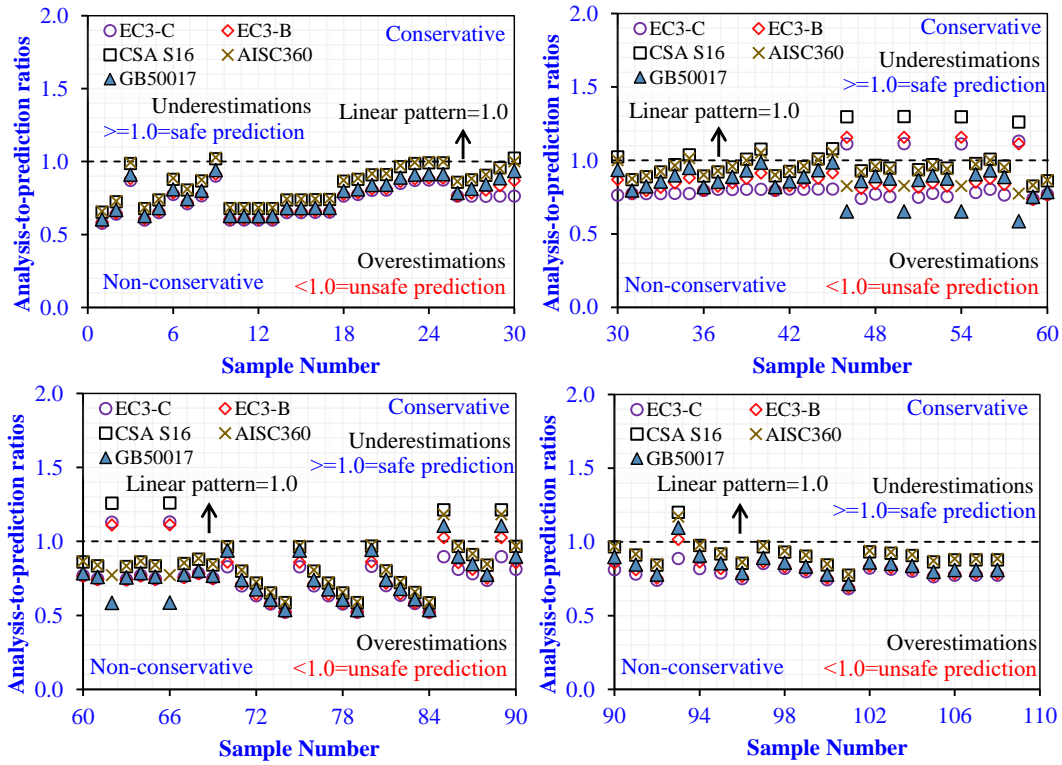
$$\phi = 0.5 [1 + \alpha(\bar{\lambda} - 0.2) + \bar{\lambda}^2]; \bar{\lambda} = \sqrt{f_y A_s / P_{cr}} \quad (7)$$

561 where  $P_{cr}$  and  $\gamma_M$  represent critical load [100] and a partial safety factor. The code  
 562 [101,102], standards [103], statistical studies [104], and research [12–14] recommend  
 563 1.0, overestimating 101 and 98 outcomes for  $P_{u,c}$  and  $P_{u,b}$ .

564 An analogous procedure has been used to draw the results with CSA S16-19 [105] and  
 565 AISC360-16 [106] that adopt a resistance factor of 0.90 [107], overestimating 90 and  
 566 96 outcomes. Similarly, the GB50017-2017 standard [79] overestimates 104 results,  
 567 with  $\alpha_1, \alpha_2,$  and  $\alpha_3$  of 0.65, 0.965, and 0.3.

## 568 5.1 Validations

569 The applicability of EC3-C, EC3-B, CSA S16, AISC360-16, and GB50017-2017 was  
 570 examined by comparing analysis-to-prediction ratios of shear-keyed tubes  $P_u$   
 571 summarized in **Table 4**. Cross-sectional ( $P_{u,c}$ ) and buckling ( $P_{u,b}$ ) resistances in EC3:1-  
 572 1 are represented as EC3-C and EC3-B. **Figure 20** demonstrates that conventional  
 573 design standards provide non-conservative outcomes with 101, 98, 90, 96, and 104  
 574 over- and 6, 9, 17, 11, and 3 under-estimations. Due to underestimating the strength,  
 575 slender cross-sections generally yielded conservative results. Thus, strength reduction  
 576 factors modifications as a function of the shear-keyed IMC and tube parameters are  
 577 required to accurately anticipate the shear-keyed tubes' compressive behavior.



Sample No	1-30		30-60		60-90		90-108		Total	
	Mean	Cov	Mean	Cov	Mean	Cov	Mean	Cov	Mean	Cov
○ EC3-C	0.73	0.14	0.82	0.14	0.74	0.20	0.79	0.06	0.77	0.16
◇ EC3-B	0.75	0.14	0.87	0.13	0.76	0.21	0.82	0.08	0.80	0.16
□ CSA S16	0.84	0.15	1.00	0.13	0.86	0.22	0.92	0.10	0.90	0.17
✕ AISC360	0.84	0.14	0.93	0.07	0.83	0.18	0.92	0.09	0.87	0.14
△ GB50017	0.77	0.15	0.85	0.12	0.76	0.20	0.85	0.10	0.80	0.15

Fig. 20 Non-modified prediction equations outcomes

578  
579  
580

## 6 Conclusions

581 This research examined shear-keyed columns' compression behaviors by evaluating  
582 the parametric effect using validated FEM. The compression resistances were  
583 estimated using conventional design standards prediction equations. This study  
584 supports the following outcomes:  
585

- 586 1. The shear-keyed columns' load-shortening behavior reveals better compressive  
587 behavior accompanied by weaker ductility with larger shear-keyed IMC  
588 (greater  $t_t$  and  $L_t$ ) and vice versa. Local buckling initiates when tubes achieve  
589 their ultimate compressive strength, causing their capacity to decline.

- 590 2. Buckling at ends is observed in long or rectangular tubes with shorter shear-key  
591 due to stress localization, whereas stub or intermediate tubes with longer shear-  
592 key shift it away from the column's ends. Local inward buckling accompanied  
593 outward, producing a sinusoidal pattern opposite on neighboring and similar on  
594 opposite faces.
- 595 3. Raising tubes and shear-key stiffening parameters increases strength and  
596 stiffness while increasing member length or slenderness ratio reduces stiffness  
597 and ductility. Longer tubes with a slender shear-key exhibit a more decrease in  
598 ductility due to slenderness or shear-key shear stresses. Capacity and stiffness  
599 dropped by raising imperfection from  $t_c/100$  to  $t_c/10$ ,  $t_c/5$ ,  $t_c/2$ , and  $t_c$ , and  
600  $L_c/2000$  to  $L_c/1500$ ,  $L_c/1000$ , and  $L_c/500$ . Increasing  $t_c/100$  to  $t_c$  raised  $\Delta_u$  but  
601 lowered  $DI$ , whereas increasing  $L_c/2000$  to  $L_c/500$  reduced  $\Delta_u$  and  $DI$ .
- 602 4. Due to shear-key influence, the capacity decreases significantly, making it  
603 challenging to achieve conservative outcomes with conventional design  
604 standards, necessitating more restrictive resistance factors based on the tube and  
605 shear-keyed IMC parameters.

606 This study focused primarily on the parametric compression behaviors of single  
607 shear-keyed tubular columns. Thus, findings are restricted to the examined models.  
608 Based on experimental, numerical, and analytical assessments, future studies will  
609 be conducted on group shear-keyed columns, i.e., four neighboring module columns,  
610 which will be more appropriate to the practical development of MSS.

## 611 **Acknowledgment**

612 The authors gratefully acknowledge financial support from the National Natural  
613 Science Foundation of China (Grant Nos. 51978457 and 52008292) and the China  
614 Scholarship Council. The authors appreciate the editors' and reviewers' efforts in  
615 providing valuable recommendations that helped us improve the quality of the  
616 manuscript.

## 617 **References**

- 618 [1] Z. Chen, K. Khan, A. Khan, K. Javed, J. Liu, Exploration of the multidirectional stability and  
619 response of prefabricated volumetric modular steel structures, *J. Constr. Steel Res.* 184 (2021)  
620 106826. <https://doi.org/10.1016/j.jcsr.2021.106826>.
- 621 [2] K. Khan, Z. Chen, J. Liu, K. Javed, State-of-the-Art on Technological Developments and  
622 Adaptability of Prefabricated Industrial Steel Buildings, *Appl. Sci.* 13 (2023).
- 623 [3] R.M. Lawson, Building design using modules, *Steel Constr. Inst.* (2007) 1–16.
- 624 [4] Y. Shahtaheri, C. Rausch, J. West, C. Haas, M. Nahangi, Managing risk in modular construction  
625 using dimensional and geometric tolerance strategies, *Autom. Constr.* 83 (2017) 303–315.  
626 <https://doi.org/10.1016/j.autcon.2017.03.011>.
- 627 [5] P.F. Court, C.L. Pasquire, G.F. Gibb, D. Bower, Modular Assembly with Postponement to  
628 Improve Health, Safety, and Productivity in Construction, *Pract. Period. Struct. Des. Constr.* 14  
629 (2009) 81–89. [https://doi.org/10.1061/\(asce\)1084-0680\(2009\)14:2\(81\)](https://doi.org/10.1061/(asce)1084-0680(2009)14:2(81)).
- 630 [6] L. Jaillon, C.S. Poon, Y.H. Chiang, Quantifying the waste reduction potential of using  
631 prefabrication in building construction in Hong Kong, *Waste Manag.* 29 (2009) 309–320.  
632 <https://doi.org/10.1016/j.wasman.2008.02.015>.
- 633 [7] J.F. Zhang, J.J. Zhao, D.Y. Yang, E.F. Deng, H. Wang, S.Y. Pang, L.M. Cai, S.C. Gao,  
634 Mechanical-property tests on assembled-type light steel modular house, *J. Constr. Steel Res.* 168  
635 (2020) 105981. <https://doi.org/10.1016/j.jcsr.2020.105981>.
- 636 [8] S.Y. Zhai, Y.F. Lyu, K. Cao, G.Q. Li, W.Y. Wang, C. Chen, Experimental study on bolted-cover  
637 plate corner connections for column-supported modular steel buildings, *J. Constr. Steel Res.* 189  
638 (2022) 107060. <https://doi.org/10.1016/j.jcsr.2021.107060>.
- 639 [9] Y.F. Lyu, G.Q. Li, K. Cao, S.Y. Zhai, Y.B. Wang, L. Mao, M. ming Ran, Bending behavior of  
640 splice connection for corner-supported steel modular buildings, *Eng. Struct.* 250 (2022) 113460.  
641 <https://doi.org/10.1016/j.engstruct.2021.113460>.
- 642 [10] Y.F. Lyu, G.Q. Li, K. Cao, S.Y. Zhai, H. Li, C. Chen, Y.Z. Wang, Behavior of splice connection  
643 during transfer of vertical load in full-scale corner-supported modular building, *Eng. Struct.* 230  
644 (2021) 111698. <https://doi.org/10.1016/j.engstruct.2020.111698>.
- 645 [11] P. Barnes, Off-site fabrication, *BIM Princ. Pract.* (2019) 109–112.  
646 <https://doi.org/10.1680/bimpp.63693.109>.
- 647 [12] K. Khan, Z. Chen, J. Liu, A. Khan, K. Javed, Axial compression behaviours of tubular sectioned  
648 C-shape continuous-supported steel walls in MSB, *J. Constr. Steel Res.* 188 (2022) 107009.  
649 <https://doi.org/10.1016/j.jcsr.2021.107009>.
- 650 [13] K. Khan, Z. Chen, J. Liu, A. Khan, Experimental and numerical study on planar multi-column  
651 walls behaviours with boundary supports, *J. Constr. Steel Res.* 186 (2021) 106880.  
652 <https://doi.org/10.1016/j.jcsr.2021.106880>.
- 653 [14] K. Khan, Z. Chen, J. Liu, A. Khan, Numerical and parametric analysis on compressive  
654 behaviours of continuous-supported wall systems in MSB, *Structures.* 33 (2021) 4053–4079.  
655 <https://doi.org/10.1016/j.istruc.2021.07.001>.
- 656 [15] R.M. Lawson, R.G. Ogden, R. Bergin, Application of Modular Construction in High-Rise  
657 Buildings, *J. Archit. Eng.* 18 (2012) 148–154. [https://doi.org/10.1061/\(asce\)ae.1943-5568.0000057](https://doi.org/10.1061/(asce)ae.1943-5568.0000057).
- 659 [16] A.W. Lacey, W. Chen, H. Hao, K. Bi, Review of bolted inter-module connections in modular

- 660 steel buildings, *J. Build. Eng.* 23 (2019) 207–219. <https://doi.org/10.1016/j.jobe.2019.01.035>.
- 661 [17] C.D. Annan, M.A. Youssef, M.H. El Naggar, Seismic overstrength in braced frames of modular  
662 steel buildings, *J. Earthq. Eng.* 13 (2009) 1–21. <https://doi.org/10.1080/13632460802212576>.
- 663 [18] Z. Chen, H. Li, A. Chen, Y. Yu, H. Wang, Research on pretensioned modular frame test and  
664 simulations, *Eng. Struct.* 151 (2017) 774–787. <https://doi.org/10.1016/j.engstruct.2017.08.019>.
- 665 [19] Y. Yu, Z. Chen, A. Chen, Experimental study of a pretensioned connection for modular buildings,  
666 *Steel Compos. Struct.* 31 (2019) 217–232. <https://doi.org/10.12989/scs.2019.31.3.217>.
- 667 [20] C. Kyung-Suk, K. Hyung-Joon, Analytical Models of Beam-Column joints in a Unit Modular  
668 Frame (in Korean), *J. Comput. Struct. Eng. Inst. Korea.* 27 (2014) 663–672.  
669 <https://doi.org/10.7734/coseik.2014.27.6.663>.
- 670 [21] M. Lawson, R. Ogden, C. Goodier, Design in Modular Construction, 2014.  
671 <https://doi.org/10.1201/b16607>.
- 672 [22] H.T. Thai, T. Ngo, B. Uy, A review on modular construction for high-rise buildings, *Structures.*  
673 28 (2020) 1265–1290. <https://doi.org/10.1016/j.istruc.2020.09.070>.
- 674 [23] Z. Ye, K. Giriunas, H. Sezen, G. Wu, D.C. Feng, State-of-the-art review and investigation of  
675 structural stability in multi-story modular buildings, *J. Build. Eng.* 33 (2021) 101844.  
676 <https://doi.org/10.1016/j.jobe.2020.101844>.
- 677 [24] S. Srisangeerthan, M.J. Hashemi, P. Rajeev, E. Gad, S. Fernando, Review of performance  
678 requirements for inter-module connections in multi-story modular buildings, *J. Build. Eng.* 28  
679 (2020) 101087. <https://doi.org/10.1016/j.jobe.2019.101087>.
- 680 [25] A.W. Lacey, W. Chen, H. Hao, K. Bi, Structural response of modular buildings – An overview,  
681 *J. Build. Eng.* 16 (2018) 45–56. <https://doi.org/10.1016/j.jobe.2017.12.008>.
- 682 [26] C. Dan-Adrian, K.D. Tsavdaridis, A comprehensive review and classification of inter-module  
683 connections for hot-rolled steel modular building systems, *J. Build. Eng.* 50 (2022) 104006.  
684 <https://doi.org/10.1016/j.jobe.2022.104006>.
- 685 [27] E.F. Deng, L. Zong, Y. Ding, Z. Zhang, J.F. Zhang, F.W. Shi, L.M. Cai, S.C. Gao, Seismic  
686 performance of mid-to-high rise modular steel construction - A critical review, *Thin-Walled*  
687 *Struct.* 155 (2020) 106924. <https://doi.org/10.1016/j.tws.2020.106924>.
- 688 [28] Z. Chen, J. Liu, Y. Yu, Experimental study on interior connections in modular steel buildings,  
689 *Eng. Struct.* 147 (2017) 625–638. <https://doi.org/10.1016/j.engstruct.2017.06.002>.
- 690 [29] Z. Chen, J. Liu, Y. Yu, C. Zhou, R. Yan, Experimental study of an innovative modular steel  
691 building connection, *J. Constr. Steel Res.* 139 (2017) 69–82.  
692 <https://doi.org/10.1016/j.jcsr.2017.09.008>.
- 693 [30] K. Khan, Z. Chen, J. Liu, J. Yan, Simplified modelling of novel non-welded joints for modular  
694 steel buildings, *Adv. Steel Constr.* (2021).
- 695 [31] K. Khan, J.B. Yan, Finite Element Analysis on Seismic Behaviour of Novel Joint in Prefabricated  
696 Modular Steel Building, *Int. J. Steel Struct.* (2020). <https://doi.org/10.1007/s13296-020-00320-w>.
- 697
- 698 [32] K. Khan, J.-B. Yan, Numerical studies on seismic behaviour of a prefabricated multi storey  
699 modular steel building with new type bolted joints, *Adv. Steel Constr.* 17(1) (2021) 1–9.  
700 <https://doi.org/10.18057/IJASC.2021.17.1.1>.
- 701 [33] J. Peng, C. Hou, L. Shen, Progressive collapse analysis of corner-supported composite buildings,  
702 *J. Build. Eng.* 48 (2022).
- 703 [34] J. Peng, C. Hou, L. Shen, Numerical analysis of composite modular buildings under wind actions,  
704 *J. Constr. Steel Res.* 187 (2021).
- 705 [35] J. Peng, C. Hou, L. Shen, Lateral resistance of multi-story modular buildings using tenon-  
706 connected inter-module connections, *J. Constr. Steel Res.* 177 (2021).
- 707 [36] J. Peng, C. Hou, L. Shen, Numerical simulation of weld fracture using cohesive interface for  
708 novel inter-module connections, *J. Constr. Steel Res.* 174 (2020).
- 709 [37] B. Hajimohammadi, S. Das, H. Ghaednia, J. Dhanapal, Structural performance of registration

- 710 pin connection in VectorBloc modular construction system, *J. Constr. Steel Res.* 197 (2022)  
711 107464. <https://doi.org/10.1016/j.jcsr.2022.107464>.
- 712 [38] J. Bowron, Locating pin assembly for a modular frame, WO2020010463A1, 2020.
- 713 [39] S.D. Pang, J.Y.R.L. Liew, Z. Dai, Y. Wang, Prefabricated Prefinished Volumetric Construction  
714 Joining Tech-niques Review, *Modul. Offsite Constr. Summit Proc.* (2016).  
715 <https://doi.org/10.29173/mocs31>.
- 716 [40] Z. Dai, T.Y.C. Cheong, S.D. Pang, J.Y.R. Liew, Experimental study of grouted sleeve  
717 connections under bending for steel modular buildings, *Eng. Struct.* 243 (2021) 112614.  
718 <https://doi.org/10.1016/j.engstruct.2021.112614>.
- 719 [41] Z. Dai, S.D. Pang, J.R. Liew, Axial load resistance of grouted sleeve connection for modular  
720 construction, *Thin-Walled Struct.* 154 (2020) 106883.  
721 <https://doi.org/10.1016/j.tws.2020.106883>.
- 722 [42] R. Ma, J. Xia, H. Chang, B. Xu, L. Zhang, Experimental and numerical investigation of  
723 mechanical properties on novel modular connections with superimposed beams, 232 (2021).  
724 <https://doi.org/10.1016/j.engstruct.2021.111858>.
- 725 [43] E.F. Deng, J.B. Yan, Y. Ding, L. Zong, Z.X. Li, X.M. Dai, Analytical and numerical studies on  
726 steel columns with novel connections in modular construction, *Int. J. Steel Struct.* 17 (2017)  
727 1613–1626. <https://doi.org/10.1007/s13296-017-1226-5>.
- 728 [44] G. Zhang, L. Xu, Z. Li, Development and seismic retrofit of an innovative modular steel structure  
729 connection using symmetrical self-centering haunch braces, *Eng. Struct.* 229 (2021) 111671.  
730 <https://doi.org/10.1016/j.engstruct.2020.111671>.
- 731 [45] G. Nadeem, N.A. Safiee, N. Abu Bakar, I. Abd Karim, N.A. Mohd Nasir, Finite element analysis  
732 of proposed self-locking joint for modular steel structures, *Appl. Sci.* 11 (2021).  
733 <https://doi.org/10.3390/app11199277>.
- 734 [46] M. Liu, Y. Wang, S. Jia, Research on the mechanical properties of new plate-inner sleeve joint  
735 of steel modular frame (in Chinese), *Steel Constr.* (2018).
- 736 [47] F. Shi, Y. Li, Innovative inner sleeve composite bolted connections for modular steel  
737 constructions: Experimental and numerical studies, *J. Build. Eng.* (2022) 105624.  
738 <https://doi.org/10.1016/j.jobe.2022.105624>.
- 739 [48] R.J. Liew, Z. Dai, Y.S. Chau, *Steel Concrete Composite Systems for Modular Construction of  
740 High-rise Buildings*, (2018). <https://doi.org/10.4995/asccs2018.2018.7220>.
- 741 [49] J.Y.R. Liew, Y.S. Chua, Z. Dai, Steel concrete composite systems for modular construction of  
742 high-rise buildings, *Structures.* 21 (2019) 135–149. <https://doi.org/10.1016/j.istruc.2019.02.010>.
- 743 [50] R. Sanches, O. Mercan, B. Roberts, Experimental investigations of vertical post-tensioned  
744 connection for modular steel structures, *Eng. Struct.* 175 (2018) 776–789.  
745 <https://doi.org/10.1016/j.engstruct.2018.08.049>.
- 746 [51] R. Sanches, O. Mercan, Vertical post-tensioned connection for modular steel buildings, (2019)  
747 1–8.
- 748 [52] A.W. Lacey, W. Chen, H. Hao, K. Bi, New interlocking inter-module connection for modular  
749 steel buildings: Experimental and numerical studies, *Eng. Struct.* 198 (2019).  
750 <https://doi.org/10.1016/j.engstruct.2019.109465>.
- 751 [53] A.W. Lacey, W. Chen, H. Hao, K. Bi, F.J. Tallowin, Shear behaviour of post-tensioned inter-  
752 module connection for modular steel buildings, *J. Constr. Steel Res.* 162 (2019) 105707.  
753 <https://doi.org/10.1016/j.jcsr.2019.105707>.
- 754 [54] K. Tayyebi, M. Sun, Design of direct-formed square and rectangular hollow section stub columns,  
755 *J. Constr. Steel Res.* 178 (2021) 106499. <https://doi.org/10.1016/j.jcsr.2020.106499>.
- 756 [55] Monash University-modular construction codes board, *Handbook for the Design of modular  
757 structures*, Monash University, 2017.
- 758 [56] M. Theofanous, *Studies of the Nonlinear Response of Stainless Steel Structures*, Imperial  
759 College London, 2010.
- 760 [57] M. Theofanous, L. Gardner, Testing and numerical modelling of lean duplex stainless steel

- 761 hollow section columns, *Eng. Struct.* 31 (2009) 3047–3058.  
762 <https://doi.org/10.1016/j.engstruct.2009.08.004>.
- 763 [58] J. Hou, X. Wang, J. Liu, Z. Chen, X. Zhong, Study on the stability bearing capacity of multi-  
764 column wall in modular steel building, *Eng. Struct.* 214 (2020) 110648.  
765 <https://doi.org/10.1016/j.engstruct.2020.110648>.
- 766 [59] ABAQUS (2013), User manual Version 6.13., DS SIMULIA Corp, Provid. RI, USA. (2013) 1–  
767 847.
- 768 [60] B.K.J.R. Rasmussen, G.J. Hancock, Stainless Steel Structural Members . Outline of Test  
769 Program, 119 (2006) 2349–2367.
- 770 [61] R.B. Cruise, L. Gardner, Residual stress analysis of structural stainless steel sections, *J. Constr.*  
771 *Steel Res.* 64 (2008) 352–366. <https://doi.org/10.1016/j.jcsr.2007.08.001>.
- 772 [62] I. Arrayago, K.J.R. Rasmussen, Influence of the imperfection direction on the ultimate response  
773 of steel frames in advanced analysis, *J. Constr. Steel Res.* 190 (2022) 107137.  
774 <https://doi.org/10.1016/j.jcsr.2022.107137>.
- 775 [63] X. Wang, J. Hou, J. Liu, Z. Tian, Study of effective length factor for column in steel multi-  
776 column wall (in Chinese), in: 18th Natl. Symp. Mod. Struct. Eng., 2018: pp. 36–40.
- 777 [64] J. Hou, Stability of Multi-column Wall in Modular Steel Structures (MS thesis in Chinese),  
778 Tianjin University, 2018.
- 779 [65] Martijn Visser, What is a stress singularity in SOLIDWORKS Simulation?, *Elit. Appl. Eng.*  
780 *CAD2M.* (2018). [https://blogs.solidworks.com/tech/2018/07/what-is-a-stress-singularity-in-](https://blogs.solidworks.com/tech/2018/07/what-is-a-stress-singularity-in-solidworks-simulation.html)  
781 [solidworks-simulation.html](https://blogs.solidworks.com/tech/2018/07/what-is-a-stress-singularity-in-solidworks-simulation.html).
- 782 [66] LESLIE LANGNAU, Avoiding singularities in FEA boundary conditions, *World (A Des. World*  
783 *Resour.* (2021). [https://www.3dcadworld.com/avoiding-singularities-in-fea-boundary-](https://www.3dcadworld.com/avoiding-singularities-in-fea-boundary-conditions/)  
784 [conditions/](https://www.3dcadworld.com/avoiding-singularities-in-fea-boundary-conditions/).
- 785 [67] Łukasz Skotny, Stress singularity – an honest discussion, *Enterfea.* (2017).  
786 <https://enterfea.com/stress-singularity-an-honest-discussion/>.
- 787 [68] H.J. Fogg, L. Sun, J.E. Makem, C.G. Armstrong, T.T. Robinson, Singularities in structured  
788 meshes and cross-fields, *CAD Comput. Aided Des.* 105 (2018) 11–25.  
789 <https://doi.org/10.1016/j.cad.2018.06.002>.
- 790 [69] Y. Pandya, A. Parey, Failure path based modified gear mesh stiffness for spur gear pair with  
791 tooth root crack, *Eng. Fail. Anal.* 27 (2013) 286–296.  
792 <https://doi.org/10.1016/j.engfailanal.2012.08.015>.
- 793 [70] M. Acin, Stress singularities, stress concentrations and mesh convergence, *Acin.Net*  
794 *(Engineering My Life).* (2015). [http://www.acin.net/2015/06/02/stress-singularities-stress-](http://www.acin.net/2015/06/02/stress-singularities-stress-concentrations-and-mesh-convergence/)  
795 [concentrations-and-mesh-convergence/](http://www.acin.net/2015/06/02/stress-singularities-stress-concentrations-and-mesh-convergence/).
- 796 [71] G. İrsel, The effect of using shell and solid models in structural stress analysis, *Vibroengineering*  
797 *Procedia.* 27 (2019) 115–120. <https://doi.org/10.21595/vp.2019.20977>.
- 798 [72] Y. Liu, G. Glass, Effects of mesh density on finite element analysis, *SAE Tech. Pap.* 2 (2013).  
799 <https://doi.org/10.4271/2013-01-1375>.
- 800 [73] J. Ye, S.M. Mojtabaei, I. Hajirasouliha, Local-flexural interactive buckling of standard and  
801 optimised cold-formed steel columns, *J. Constr. Steel Res.* 144 (2018) 106–118.  
802 <https://doi.org/10.1016/j.jcsr.2018.01.012>.
- 803 [74] D.S. Castanheira, L.R.O. De Lima, P.C.G. Da Silva Vellasco, A.T. Da Silva, M.C. Rodrigues,  
804 Numerical modelling of rectangular cold-formed steel and composite columns, *Proc. Inst. Civ.*  
805 *Eng. Struct. Build.* 172 (2019) 805–818. <https://doi.org/10.1680/jstbu.18.00057>.
- 806 [75] B. Xu, J. Xia, R. Ma, J. Wang, X. Chen, H. Chang, L. Zhang, Investigation on true stress-strain  
807 curves of flat and corner regions of cold-formed section using 3D digital image correlation  
808 method, *Adv. Civ. Eng.* 2019 (2019). <https://doi.org/10.1155/2019/3138176>.
- 809 [76] E. 1993-1-5, Eurocode 3 - Design of steel structures - Part 1-5: Plated structural elements, 2006.
- 810 [77] J.B. Yan, J. Feng, Y.B. Luo, Y. Du, Compression behaviour of stainless-steel stub square tubular  
811 columns at cold-region low temperatures, *J. Constr. Steel Res.* 187 (2021).

- 812 <https://doi.org/10.1016/j.jcsr.2021.106984>.
- 813 [78] Y. Du, M. Fu, Z. Chen, J.B. Yan, Z. Zheng, Axial compressive behavior of CFRP confined  
814 rectangular CFT columns using high-strength materials: Numerical analysis and carrying  
815 capacity model, *Structures*. 36 (2022) 997–1020. <https://doi.org/10.1016/j.istruc.2021.12.061>.
- 816 [79] GB50017-2017, Standard for design of steel structures (in Chinese), (2017).
- 817 [80] Y. Chen, C. Hou, J. Peng, Stability study on tenon-connected SHS and CFST columns in modular  
818 construction, *Steel Compos. Struct.* 30 (2019) 185–199.  
819 <https://doi.org/10.12989/scs.2019.30.2.185>.
- 820 [81] A.W. Lacey, W. Chen, H. Hao, Experimental methods for inter-module joints in modular  
821 building structures – A state-of-the-art review, *J. Build. Eng.* 46 (2022) 103792.  
822 <https://doi.org/10.1016/j.jobe.2021.103792>.
- 823 [82] R. Sanches, O. Mercan, B. Roberts, Experimental investigations of vertical post-tensioned  
824 connection for modular steel structures, *Eng. Struct.* 175 (2018) 776–789.  
825 <https://doi.org/10.1016/j.engstruct.2018.08.049>.
- 826 [83] ASTM, Grade Q345 Imported Tube does not conform to grade S355 | Association of Steel Tube  
827 and Pipe Manufacturers, (n.d.). <https://www.astpm.com/grade-q345-imported-tube-does-not-conform-to-grade-s355/> (accessed April 24, 2021).
- 829 [84] K. Rzeszut, Post-Buckling Behaviour of Steel Structures with Different Types of Imperfections,  
830 *Appl. Sci.* 12 (2022). <https://doi.org/10.3390/app12189018>.
- 831 [85] J. Yan, B. Zhang, X. Yu, J. Xie, Thin-Walled Structures Mechanical properties of stainless steel  
832 QN1906Mo at sub-zero temperatures : Tests and stress – strain models, *Thin-Walled Struct.* 179  
833 (2022) 109727. <https://doi.org/10.1016/j.tws.2022.109727>.
- 834 [86] J.B. Yan, Y.L. Luo, C. Liang, X. Lin, Y.B. Luo, L. Zhang, Compression behaviours of concrete-  
835 filled Q690 high-strength steel tubular columns at low temperatures, *J. Constr. Steel Res.* 187  
836 (2021) 106983. <https://doi.org/10.1016/j.jcsr.2021.106983>.
- 837 [87] J.B. Yan, X. Yang, Y. Luo, P. Xie, Y.B. Luo, Axial compression behaviours of ultra-high  
838 performance concrete-filled Q690 high-strength steel tubes at low temperatures, *Thin-Walled  
839 Struct.* 169 (2021) 108419. <https://doi.org/10.1016/j.tws.2021.108419>.
- 840 [88] J.B. Yan, T. Wang, X. Dong, Compressive behaviours of circular concrete-filled steel tubes  
841 exposed to low-temperature environment, *Constr. Build. Mater.* 245 (2020) 118460.  
842 <https://doi.org/10.1016/j.conbuildmat.2020.118460>.
- 843 [89] J.B. Yan, W.J. Xie, Y. Luo, T. Wang, Behaviours of concrete stub columns confined by steel  
844 tubes at cold-region low temperatures, *J. Constr. Steel Res.* 170 (2020) 106124.  
845 <https://doi.org/10.1016/j.jcsr.2020.106124>.
- 846 [90] J.B. Yan, X. Dong, T. Wang, Axial compressive behaviours of square CFST stub columns at low  
847 temperatures, *J. Constr. Steel Res.* 164 (2020) 105812.  
848 <https://doi.org/10.1016/j.jcsr.2019.105812>.
- 849 [91] J.B. Yan, Y.L. Luo, L. Su, X. Lin, Y.B. Luo, L. Zhang, Low-temperature compression behaviour  
850 of square CFST columns using Q960 ultra-high strength steel, *J. Constr. Steel Res.* 183 (2021).  
851 <https://doi.org/10.1016/j.jcsr.2021.106727>.
- 852 [92] M.X. Xiong, J.B. Yan, Buckling length determination of concrete filled steel tubular column  
853 under axial compression in standard fire test, *Mater. Struct. Constr.* 49 (2016) 1201–1212.  
854 <https://doi.org/10.1617/s11527-015-0570-1>.
- 855 [93] H. Chen, C. Ke, C. Chen, G. Li, Study on the shear behavior of inter-module connection with a  
856 bolt and shear key fitting for modular steel buildings, 0 (2022) 1–16.  
857 <https://doi.org/10.1177/13694332221122547>.
- 858 [94] J. Wang, B. Uy, D. Li, Analysis of demountable steel and composite frames with semi-rigid  
859 bolted joints, *Steel Compos. Struct.* 28 (2018) 363–380.  
860 <https://doi.org/10.12989/scs.2018.28.3.363>.
- 861 [95] Z. Xu, T. Zayed, Y. Niu, Comparative analysis of modular construction practices in mainland  
862 China, Hong Kong and Singapore, *J. Clean. Prod.* 245 (2020).  
863 <https://doi.org/10.1016/j.jclepro.2019.118861>.

- 864 [96] A. Shapoval, V. Courtillot, Influence of the P-delta Effect and Stiffness Irregularity on the  
865 Structural Behavior of Reinforced Concrete Buildings Influence of the P-delta Effect and  
866 Stiffness Irregularity on the Structural Behavior of Reinforced Concrete Buildings, in: J. Phys.  
867 Conf. Ser., IOP, 2022. <https://doi.org/10.1088/1742-6596/2287/1/012047>.
- 868 [97] J.B. Yan, X. Dong, J.S. Zhu, Behaviours of stub steel tubular columns subjected to axial  
869 compression at low temperatures, *Constr. Build. Mater.* 228 (2019).  
870 <https://doi.org/10.1016/j.conbuildmat.2019.116788>.
- 871 [98] T.G. Singh, T. Chan, Effect of access openings on the buckling performance of square hollow  
872 section module stub columns, *J. Constr. Steel Res.* 177 (2021) 106438.  
873 <https://doi.org/10.1016/j.jcsr.2020.106438>.
- 874 [99] EN 1993-1-1, Eurocode 3: Design of steel structures - Part 1-1: General rules and rules for  
875 buildings, 2005.
- 876 [100] L. Srikanth, Design of steel structures based on BS5950, 2020.  
877 <https://doi.org/10.13140/RG.2.2.25897.75364>.
- 878 [101] UK steel construction information, Member design - SteelConstruction.info, (n.d.).  
879 [https://www.steelconstruction.info/Member\\_design#cite\\_note-NAtoBSEN1993-1-1-2](https://www.steelconstruction.info/Member_design#cite_note-NAtoBSEN1993-1-1-2)  
880 (accessed June 11, 2021).
- 881 [102] NA to CYS EN 1993-1-1:2005, Eurocode 3: Design of steel structures Part 1-1: General rules  
882 and rules for buildings, 2005 (2014).
- 883 [103] B. Charbrolin, Technical steel research-Partial safety factors for resistance of steel elements to  
884 EC3 and EC4 — Calibration for various steel products and failure criteria, 2002.
- 885 [104] Publications Office of the EU, Partial safety factors for resistance of steel elements to EC3 and  
886 EC4 - Calibration for various steel products and failure criteria, (n.d.).  
887 [https://op.europa.eu/en/publication-detail/-/publication/1602ab5d-3994-4464-8c44-](https://op.europa.eu/en/publication-detail/-/publication/1602ab5d-3994-4464-8c44-664016689b1e)  
888 [664016689b1e](https://op.europa.eu/en/publication-detail/-/publication/1602ab5d-3994-4464-8c44-664016689b1e) (accessed June 19, 2021).
- 889 [105] CSA-S16-09, CSA standard-Design of steel structures, 2009.
- 890 [106] ANSI/AISC 360-16, AISC360/16 Specification for Structural Steel Buildings-An American  
891 National Standard, 2016.
- 892 [107] S. Pinarbasi, T. Genc, E. Akpınar, F. Okay, Comparison of Design Guidelines for Hot-Rolled I-  
893 Shaped Steel Compression Members according to AISC 360-16 and EC3, *Adv. Civ. Eng.* 2020  
894 (2020). <https://doi.org/10.1155/2020/6853176>.
- 895

896 **Nomenclature**

897 IMC, inter-modular connections; MSS, modular steel structure; TSS, traditional steel structures;  
898 SHS, steel-hollow sections; HSS, high strength steel;  $a_c$ , elliptical tube's longest diameter;  $b_c$ ,  
899 elliptical tube's shortest diameter;  $D$ , tube's length;  $B$ , tube's width;  $r$ , cross-section root  
900 radii;  $L_c$ , tube's height;  $L_c/r$ , member slenderness ratio;  $t_c$ , tube's thickness;  $d$ , shear-key  
901 length;  $b$ , shear-key width;  $t_t$ , shear-key thickness;  $L_t$ , shear-key height;  $D/t_c$ , cross-  
902 sectional slenderness ratio; FEM/FEA, finite element model/analysis;  $E_s$ , tube elastic  
903 modulus;  $f_y$ , tube yield strength;  $f_u$ , tube ultimate strength;  $E_{s,w}$ , tubes' flat wall elastic  
904 modulus;  $f_{y,w}$ , tubes' flat wall yield strength;  $f_{u,w}$ , tubes' flat wall ultimate strength;  $E_{s,c}$ ,  
905 stainless tubes' corner elastic modulus;  $f_{y,c}$ , stainless tubes' corner yield strength;  $f_{u,c}$ ,  
906 stainless tubes' corner ultimate strength;  $P_u$ , ultimate compressive resistance;  $P_y$ , yield  
907 resistance;  $P_{cr}$ , critical load;  $P_{u,c}$ , ultimate cross-sectional resistance via EC3:1-1,  
908 represented as EC3-C;  $P_{u,b}$ , ultimate members buckling resistance via EC3:1-1,  
909 described as EC3-B;  $P_{u,Test}$ , ultimate resistance via test;  $P_{u,FE}$ , ultimate resistance via  
910 FEA;  $P_{u,EC3}$ , ultimate compressive resistance via EC3:1-1;  $P_{u,AISC}$ , ultimate  
911 compressive resistance via AISC360-16;  $P_{u,CSA}$ , ultimate compressive resistance via  
912 CSA S16;  $P_{u,GB}$ , ultimate compressive resistance via GB50017;  $K_e$ , initial stiffness;  $\Delta_u$ ,  
913 axial shortening;  $DI$ , ductility index;  $P_{45\%}$ , 45% load of  $P_u$ ;  $\Delta_{45\%}$ , axial shortening at  
914  $P_{45\%}$ ;  $\Delta_{85\%}$ , axial shortening at  $P_{85\%}$ ; Cov, coefficient of variation;  $e$ , eccentricity; GB,  
915 global buckling; IB, inward buckling; OB, outward buckling;  $\sigma_T/\sigma_E$  = True/Engineering  
916 stress;  $\varepsilon_T/\varepsilon_E$  = True/Engineering strain;  $\gamma_M$ , partial safety factor in EC3:1-1;  
917  $\alpha_1$ ,  $\alpha_2$ , and  $\alpha_3$ , partial safety factors in GB50017  
918